JFM PAPERS

Sensitivity and downstream influence of the impinging leading-edge vortex instability in a bileaflet mechanical heart valve

Hadi Zolfaghari[1],†, **Rich R. Kerswell**[1], **Dominik Obrist**[2] **and Peter J. Schmid**[3]

[1]Department of Applied Mathematics and Theoretical Physics, Centre for Mathematical Sciences, University of Cambridge, Cambridge CB3 0WA, UK

[2]ARTORG Center for Biomedical Engineering Research, University of Bern, 3010 Bern, Switzerland

[3]Department of Mathematics, Imperial College London, London SW7 2AZ, UK

Bileaflet mechanical heart valves (BMHV) create unphysiological turbulent flow. Such turbulent flow involves multiple instability mechanisms interacting with one another in a confined geometry. For instance, an impinging leading-edge vortex (ILEV) instability creates disturbances at the leading edge of the valve leaflets, while potentially promoting turbulence downstream of the BMHV (Zolfaghari and Obrist, *Phys. Rev. Fluids*, vol. 4, 2019). In this article, we use adjoint-based methods to study the structural sensitivity of the ILEV instability in the BMHV, and to quantify the role of this instability in the maximum disturbance energy growth in the wake of the BMHV. We first present a direct numerical simulation to show the effect of the ILEV instability on the turbulent flow in the wake of the valve. Second, we perform a modal linear stability analysis on a two-dimensional subdomain attached to the leading edge of one leaflet. We investigate the sensitivity of the global modes associated with this flow using their adjoints, and then show a passive control scenario using a local feedback source. This results in a partial improvement in the flow oscillations downstream of the leaflets. We finally present a non-modal approach to identify the optimal initial conditions for achieving maximum energy growth at arbitrary locations. We show that, for sufficiently large times, the optimal initial condition for highest energy growth in the wake points at the leading edge, which includes the ILEV instability. Our study illustrates that an improved leading-edge shape can effectively reduce turbulence in the wake of the BMHV.

† Email address for correspondence: hz382@cam.ac.uk

936 A41-1

1. Introduction

1.1. *Physiological background*

The aortic valve regulates the oxygenated blood flow from the heart to the rest of the organs. This valve is located between the left ventricle and the aorta, and possesses three flexible cusps. Diseases of the aortic valve make up a significant portion of valvular heart diseases (Iung & Vahanian 2011), which mainly involve thickening of the valve cusps (aortic stenosis). In severe conditions, the diseased valve must be replaced by a prosthetic valve (Yoganathan, He & Casey 2004; Sotiropoulos, Le & Gilmanov 2016).

One example of widely used prosthetic heart valves is the bileaflet mechanical heart valve (BMHV). This consists of two semi-elliptical metallic plates which regulate blood flow by pivoting in a ring-shaped housing frame (see figure 1*a*). These valves are favoured for younger patients thanks to their high durability. However, BMHVs are associated with high risk of blood clotting, for which the recipients of these valves should receive life-long blood thinning drugs to combat the risk of stroke. Shear-induced platelet activation (Holme *et al.* 1997; Alemu & Bluestein 2007), which is linked to turbulent blood flow in the valve, has been attributed to the platelet activation process. It is therefore beneficial to improve the flow in BMHVs, perhaps through design modifications, to mitigate the risk of blood clotting and stroke. Recent efforts in this area include passive control via deploying vortex generators (Hatoum & Dasi 2019) or superhydrophobic surfaces (Hatoum *et al.* 2020) on the valve leaflets, both with the goal of reducing the intensity of turbulent flow downstream of the valve.

1.2. *Brief overview of BMHV fluid mechanics*

The fluid mechanics of BMHVs have been previously studied using experimental (Ge *et al.* 2008; Bellofiore, Donohue & Quinlan 2011; Haya & Tavoularis 2016) and computational (Dasi *et al.* 2007; Borazjani, Ge & Sotiropoulos 2008; Yun *et al.* 2014*b*) investigations. These studies revealed a complex flow scenario including multiple instability mechanisms interacting in a confined and complex geometry. The flow in the wake of the valve is described as chaotic or turbulent, which has been attributed with shear-induced platelet activation risk in the bulk flow as well as in the hinge area of these prostheses (Yun *et al.* 2012; Hedayat, Asgharzadeh & Borazjani 2017; Hedayat & Borazjani 2019). Hedayat *et al.* (2017) showed that the platelet activation potential was significantly higher for BMHVs than bioprosthetic valves (i.e. valves with soft tissue cusps to mimic the native valve) at peak flow. They speculated that this could be due to the larger extent of small-scale structures for this flow. In addition to platelet activation, the relation of a flow rich in small-scale vortices and red blood damage has been studied by Quinlan & Dooley (2007). Their results showed that the root mean square of the fluid stress on cells is at least an order of magnitude less than the Reynolds stress, which is in line with the hypothesis that smaller flow eddies cause more stress on the blood cells.

The importance of vortical or turbulent flows to the forces exerted on blood components demands more investigation of the mechanisms of laminar–turbulent transition in flow through BMHVs. This can provide a more in-depth understanding of the turbulent flow and also point towards efficient ways to delay or reduce turbulence in these prostheses. Despite this importance, little attention has been paid to this area, perhaps due to the complexity of the flow. Dasi *et al.* (2007) used experimental and numerical tools to study the vorticity dynamics in a BMHV. They discussed the resulting coherent structures such as vortex rings and shear-layer instabilities, but the quantitative underpinnings of disturbance growth mechanisms leading to these vorticity phenomena were not addressed.

(*a*)

(*b*)
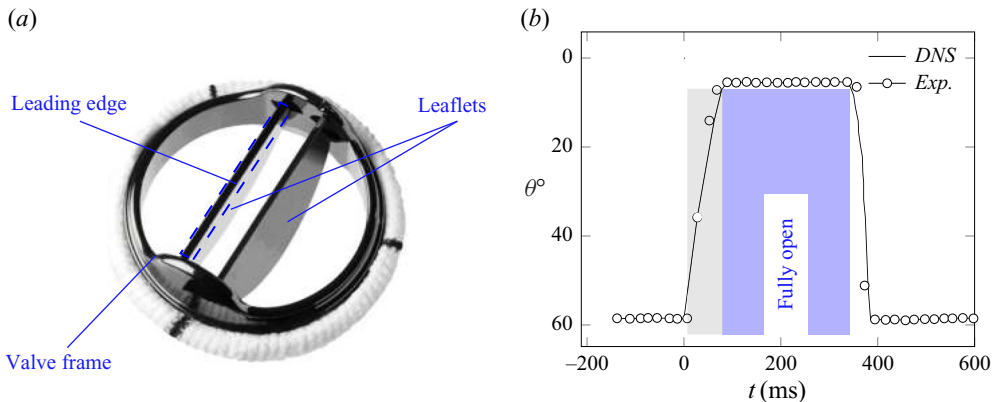
Figure 1. (*a*) Leading-edge view of a Regent mechanical valve (https://www.structuralheartsolutions.com). The valve leaflets are hinged within a metal frame housing, which is sutured to the aortic root. (*b*) Leaflet kinematics of BMHV: (–) numerical fluid–structure interaction simulation of Borazjani *et al.* (2008) and (○) experimental investigation of Dasi *et al.* (2007). The shaded area in blue shows the interval in which the valve is fully open, while the shaded area in grey shows the valve opening phase.

Bellofiore *et al.* (2011) conducted a more elaborate experimental study using up-scaled model of the valve. Using specific flow probes located downstream of the leaflets, they reported principal frequencies by calculating the frequency spectrum for an impulsively started flow as well as a systolic waveform. Based on their up-scaled model, they reported flow field data at higher spatial and temporal resolutions compared with experiments at physiologic scales. In particular, their results showed vortices entering the wake of the valve from within the leaflets, but the origin of these vortices was not investigated. They reported shedding frequencies as high as 152 Hz ($St = 0.23$, based on the projection of the leaflet length on the cross-stream plane and maximum free-stream velocity). Time history of velocity fluctuations showed that the peak frequency corresponds to peak flow time and locations downstream of the leaflets' central orifice. Motivated by this outcome and by the existing insight on flow around blunt plates in canonical settings (Hourigan, Thompson & Tan 2001), Zolfaghari & Obrist (2019) investigated the potential source of the high-velocity disturbances in the wake of the BMHV. Resorting to a bottom-up approach and employing a two-dimensional submodel, they showed that the impinging leading-edge vortex (ILEV) instability has a strong influence on the breakdown to chaotic flow in the wake of the valve.

1.3. *ILEV instability in BMHVs*

BMHV leaflets are mounted at a low angle of incidence (5°) during a significant part of a typical heartbeat (Borazjani *et al.* 2008). Because the Reynolds number (based on the aortic diameter and the mean inflow velocity at peak flow rate) can reach values as high as $Re = 10\,000$, this flow configuration becomes highly susceptible to developing an ILEV instability (Deniz & Staubli 1997; Hourigan *et al.* 2001) downstream of the leaflets' leading edges. The ILEV instability has been addressed using several canonical configurations (i.e. usually horizontal blunt plates at different chord-to-thickness aspect ratios and Reynolds numbers). These studies reveal a complex mixture of convective and absolute instabilities (Soria & Wu 1992), which could significantly affect the flow downstream of the trailing edge of these plates (Naudascher & Wang 1993). Having noticed these findings, Zolfaghari & Obrist (2019) investigated the local linear instability of the ILEV flow scenario in the BMHV. Using a two-dimensional submodel justified by

the shape of the BMHV leaflets, unstable temporal Orr–Sommerfeld modes were obtained for this flow. The cusp map procedure (Kupfer, Bers & Ram 1987) was then applied to the velocity profiles in the ILEV zone, where a pocket of absolute instability was identified. It was shown by means of two-dimensional (2-D) direct numerical simulation (DNS) that the absolute instability (wave maker) could be eliminated using a suitable modification of the leaflet's shape, which subsequently preserved the laminar flow in the wake of the BMHV.

1.4. *Scope and structure of the present work*

Although the 2-D DNS of Zolfaghari & Obrist (2019) and experimental investigations of Bellofiore *et al.* (2011) both show incoming vortices from the central orifice causing high-frequency flow oscillations and small-scale flow structures, it is useful to reproduce these phenomena using 3-D DNSs. Taking into account the complex 3-D structure of the valve leaflets not only enhances our view regarding turbulent flow in the wake of the valve, but also reveals the structure of primary mechanisms at the leading edges of the leaflets.

From a hydrodynamic stability standpoint, even though the work of Zolfaghari & Obrist (2019) provides insight on local parallel flow instabilities of ILEV structures in BMHV, a 2-D global analysis is needed to further demonstrate the 2-D spatial structure of this instability. The use of global instability analysis (Theofilis 2011) allows a more targeted geometric design effort for ameliorating turbulent flow in the wake of the BMHV. Finally, both the local parallel and the 2-D global instability analyses only consider the ILEV zone and disregard the effect of other wave makers in the system. It is thus important to re-evaluate the role of the ILEV instability in disturbance energy growth in comparison with other driving mechanisms such as the flow in the cavities. To this end, a gradient-based approach will be chosen as it can quantify whether instability growth in the wake area is more strongly promoted by the ILEV instability mechanism or by alternative and competing mechanisms.

In this present study, we first present a 3-D DNS of systolic BMHV flow. We model the systolic flow within a 3-D model, which involves fully open leaflets following the kinematic assumptions given in Zolfaghari & Obrist (2019) and Bellofiore *et al.* (2011). We make use of our in-house multi-GPU data-parallel incompressible Navier–Stokes solver (Zolfaghari & Obrist 2021) for generating the DNS data at very high resolution (a total of 337 644 801 grid points were used). This simulation was completed in 3 days on 20 GPUs of the Cray XC40/50 (*Piz Daint*). An equivalent simulation using our massively parallel CPU-based solver (Henniger, Obrist & Kleiser 2010*b*) would have taken 1.5 years to complete with equivalent compute node resources. To our knowledge, this is by far the highest grid resolution that has been used in a heart-valve simulation. The velocity fields and the Lagrangian coherent structures show the complex nature of ILEV instabilities and demonstrate the role these instabilities play in the onset and intensity of turbulent flow past the valve.

Second, a 2-D global linear instability formulation is developed (Theofilis 2011) for a subdomain attached to the leading edge of only one leaflet. The considered area was sufficiently large to cover the full extent of the time-averaged ILEV. We calculated the temporally unstable modes of this flow by performing a temporal Fourier decomposition of the linearised Navier–Stokes equations (LNSE). Two zero-frequency unstable global modes were identified. Furthermore, we calculated the adjoint of these global modes to obtain their structural sensitivity to the local momentum feedback sources (Hill 1992; Giannetti & Luchini 2007). Regions of high sensitivity were concentrated over

the wave-maker zone for one mode (mode A), while high sensitivities were also found upstream of the wave-maker zone for the second mode (mode B). This could be related, although not shown here, to the capability of the wave maker itself to amplify the disturbances (mode A), as well as cooperation of the wave maker and base flow (which includes recirculation over the wave-maker zone) to amplify or weaken the unstable mode (mode B). Using the sensitivity fields, we attempted to stabilise the flow by introducing local momentum feedback sources. To this end, small bluff bodies were introduced at areas of high structural sensitivity, and the effectiveness of these scenarios was tested using 2-D DNS. This approach failed for mode A, as expected, because its region of high sensitivity was relatively far from the wall. As a result, the introduced bluff body created more instability owing to the high Reynolds number of the flow. However, the same approach worked well for mode B, where it resulted in reduced flow oscillations between and downstream of the leaflets.

Third, we examine the effect of ILEV instability on energy growth downstream of the instability source, particularly near the trailing edge and in the wake of the valve. We resort to the 2-D submodel of Zolfaghari & Obrist (2019) and develop a gradient-based procedure to obtain optimal initial conditions for achieving maximum disturbance energy growth for specific locations in the flow. The LNSE are solved over the full domain, so that possible contributions of other instability mechanisms in the system can be accounted for. We define a cost functional to maximise the energy growth within a user-defined geometric mask and to simultaneously constrain the magnitude of the initial energy. After validating the adjoint looping formulation using transient growth calculations for plane channel flow at $Re = 3000$ (Reddy & Henningson 1993), we performed iterative direct–adjoint looping simulations using various masks at various times. It was found that for sufficiently large times the optimal initial conditions for maximum disturbance energy growth are focused around the leading edge of the leaflet, including the ILEV zone. This was further confirmed for masks that were located between the leaflets (high probability of ILEV contribution), at the trailing edge of the leaflets, and in the wake of the valve. The latter case required more time to reveal the leading-edge instability signature, which was more apparent closer to the instability source, i.e. between the leaflets.

2. Direct numerical simulation

We model the flow with the non-dimensional Navier–Stokes equations for incompressible flow

$$\frac{\partial \tilde{\boldsymbol{u}}}{\partial t} + \tilde{\boldsymbol{u}} \cdot \nabla \tilde{\boldsymbol{u}} = -\nabla \tilde{p} + \frac{1}{Re}\nabla^2 \tilde{\boldsymbol{u}} + \tilde{\boldsymbol{f}}, \quad \nabla \cdot \tilde{\boldsymbol{u}} = 0, \qquad (2.1a,b)$$

where $\tilde{\boldsymbol{u}}$ denotes the velocity field, $\tilde{p}$ stands for pressure and $\tilde{\boldsymbol{f}}$ is the body force density (non-dimensional quantities are indicated by $\tilde{\cdot}$). The Reynolds number is defined as

$$Re = \frac{\mathscr{U}_0 \mathscr{L}_0}{\nu}, \qquad (2.2)$$

where $\mathscr{U}_0 = 0.75 \, \text{m s}^{-1}$ (one half of the inflow velocity at peak flow rate,), $\mathscr{L}_0 = 3 \times r_r = 36 \, \text{mm}$ (three times the aortic root radius) and $\nu = 2.7 \times 10^{-6} \, \text{m}^2 \, \text{s}^{-1}$ are the velocity scale, length scale and the kinematic viscosity ($\nu = \rho/\mu$), respectively.

The equations (2.1a,b) are solved using a sixth-order finite-difference scheme in space on a staggered Cartesian grid, and a third-order explicit low-storage Runge–Kutta scheme in time (Henniger *et al.* 2010b; Zolfaghari *et al.* 2019; Zolfaghari & Obrist 2021). The solver has been exhaustively validated and used to study various transitional flows

(Henniger, Kleiser & Meiburg 2010*a*; Obrist, Henniger & Kleiser 2012; John, Obrist & Kleiser 2014, 2016). For integrating complex surfaces (e.g. valve leaflets) into the Cartesian grid solver, sharp-interface immersed boundary techniques are used (Mittal & Iaccarino 2005; Mittal *et al.* 2008; Zolfaghari, Izbassarov & Muradoglu 2017).

2.1. *Configuration of the numerical simulation*

2.1.1. *Kinematic assumptions*

The kinematics of the BMHV leaflets (figure 1*b*) consist of a rapid opening ($\Delta t \approx$ 20–50 ms) at the onset of systole (Vennemann *et al.* 2018), a longer phase ($\Delta t \approx 350$ ms for a typical heart rate at rest) where the leaflets remain in the open position and a rapid closing ($\Delta t \approx 25$ ms) (Dasi *et al.* 2007; Borazjani *et al.* 2008; Yun *et al.* 2014*a*). The valve leaflets remain fully open at a low angle of incidence ($5°$) during a large part of systole, which provides a suitable configuration for the creation of ILEV instabilities, as for larger angles of incidence the flow features will differ markedly from ILEV (Deniz & Staubli 1997). Starting from the time instant that the leaflets are fully open, we focus on the systolic acceleration phase, which spans approximately 200 ms. Similar to Bellofiore *et al.* (2011) and following additional justifications presented in Zolfaghari & Obrist (2019), we assume that the leaflets are fixed at an angle of $\theta = 5°$.

2.1.2. *Three-dimensional aortic root and valve model*

We define our 3-D model, as an extension of the 2-D model used in Zolfaghari & Obrist (2019). We place the leaflets of a bileaflet mechanical heart valve in the fully open position (position 1 in black colour in figure 2*a*). The sinuses of Valsalva are included in the 3-D model as three spherical cavities with a radius of r_s (figure 2*b*, bottom). The centres of these cavities are located on the $x = 0$ plane and fall on the sides of an equilateral triangle, to which the aortic root's cross-section is circumscribed. Leaflets of the BMHV are modelled as blunt plates with a triangular leading- and trailing-edge geometry (figure 2*a*). The spanwise view of the leaflets is provided on the top panel of figure 2(*b*). The model geometry resembles the semi-elliptical trailing edge of a Regent BMHV. The leaflets' thickness faces at leading and trailing edges follow the same geometry as this prosthesis. The main differences between the 3-D model geometry and a Regent BMHV are the absence of the housing ring and the valve ear/hinge recess in the 3-D model. However, these differences are located far from the centreline, hence they are not expected to notably affect the bulk flow downstream of the central orifice which is of interest in this paper.

2.1.3. *Boundary conditions and flow forcing*

The flow is smoothly accelerated from zero to the mean velocity of $\mathscr{U}_{in} = 2\mathscr{U}_0$ at $t = 200$ ms (figure 3). No-slip boundary conditions are imposed via an immersed boundary method on the rigid valve leaflets and aortic root boundaries. Periodic boundary conditions are specified in the streamwise direction x, where the systolic waveform is forced using a fringe region technique (Nordström, Nordin & Henningson 1999) upstream of the valve

$$\tilde{\boldsymbol{f}} = \lambda(\boldsymbol{x})(\tilde{\boldsymbol{u}} - \tilde{\boldsymbol{u}}_0(t)), \tag{2.3}$$

where $\lambda(\boldsymbol{x})$ is the fringe function and $\tilde{\boldsymbol{u}}_0(t)$ is a uniform flow profile. The amplitude of $\tilde{\boldsymbol{u}}_0(t)$ and the fringe function $\lambda(\boldsymbol{x})$ are tuned *ad hoc* to provide the desired systolic flow acceleration (figure 3). The fringe region forces the appropriate inflow profile, and
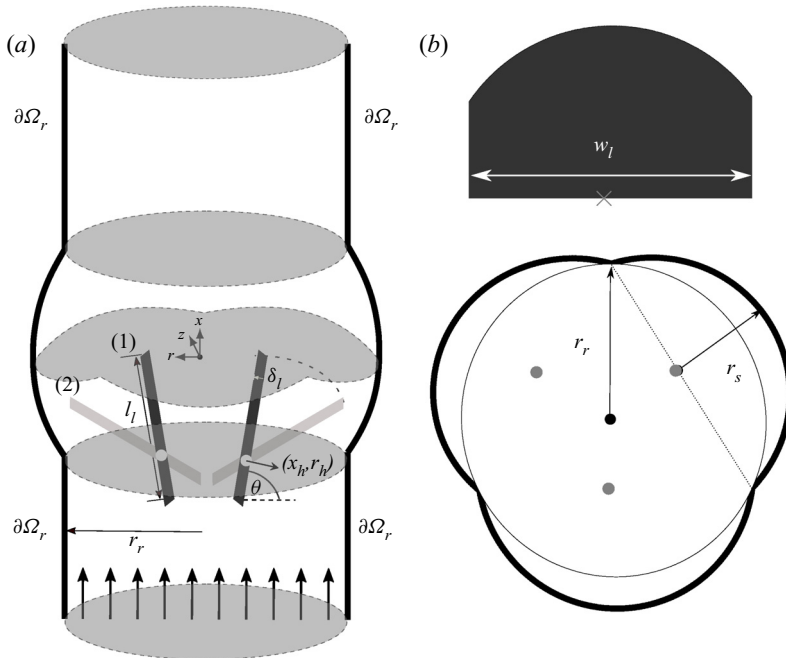
Figure 2. (*a*) A 3-D model of the BHMV in the aortic root. The 2-D cross-sections of leaflets in their plane of symmetry are shown in (1) open and (2) closed positions. (*b*, bottom) The cross-section of the root model at $x = 0$ is shown. The three grey solid points indicate the centres of the spherical cavities representing the sinuses of the Valsalva. These cavities are positioned on the centres of the sides of an equilateral triangle, to which the aortic root cross-section is circumscribed ($r_s = r_r\sqrt{3}/2$). (*b*, top) The geometry of the leaflet in the spanwise direction. The spanwise profile of the leading edge of the leaflet is modelled as a semicircle whose centre is located on the domain's axis of symmetry and on the leading edge (grey cross mark), and has a radius of l_l. All geometrical parameters of the model except those related to the cavities are given in table 1.

Parameter	Notation	Value
Root radius	r_r	12 mm
Sinus radius	r_s	$0.86r_r$
Leaflet length	l_l	$1.15r_r$
Leaflet spanwise length	w_l	$1.963r_r$
Leaflet thickness	δ_l	$0.09r_r$
Hinge longitudinal position	x_h	$-1.062r_r$
Hinge radial position	r_h	$-0.19r_r$

Table 1. Geometrical parameters of the 3-D model.

simultaneously damps out the outflow disturbances re-entering the domain at the domain's inlet due to periodic boundary conditions.

A highly resolved numerical simulation using $2561 \times 513 \times 257 = 337\,644\,801$ degrees of freedom in a cuboid domain of size $3r_r \times 3r_r \times 15r_r$ is performed. Such a high spatial resolution is set to deal with the non-conforming geometry of the leaflets, and also to resolve the spatio-temporal instability waves and their interactions (refer to the effect of grid resolution in Zolfaghari & Obrist 2021). Grid stretching is applied in all three directions, so that a grid resolution similar to the one reported by Zolfaghari & Obrist
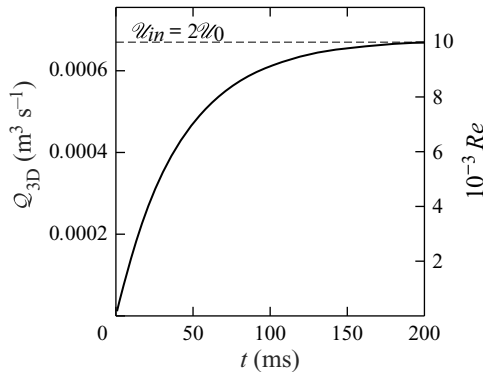
Figure 3. Acceleration part of the waveform used in the DNS. The horizontal dashed line marks the peak flow rate, corresponding to a mean flow velocity $\mathscr{U}_{in} = 2\mathscr{U}_0$.

(2019) is achieved near the leaflets (31 grid points are placed along each leaflet's thickness length δ_l). A dimensionless time-step size of $dt = 10^{-4}$ was set, and a total of 29.1K time steps were integrated (up to the physical time of $t \approx 200$ ms). To the best of our knowledge, this is the highest resolution that has been used for a numerical simulation of BMHV flow using the incompressible Navier–Stokes equations. This simulation was completed using our novel hybrid multi-GPU task and data parallel Navier–Stokes solver on 20 GPUs in three days. Because our GPU-based implementation is approximately 150 times faster than the CPU-based MPI-parallel flow solver (using the same node configuration, i.e. 20 nodes of Cray XC40/50, *Piz Daint*), the present simulation ported onto an equivalent number of CPU cores ($20 \times 16 = 320$ cores with hyper-threading) would have taken approximately 1.5 years to complete. The size of each data output of the velocity field amounted to ≈8.1 GB. Further details on this DNS and the numerical and parallelisation methodologies can be found in Zolfaghari & Obrist (2021).

2.2. *Highly resolved flow structures in the valve model*

The growth and instability of the ILEV structures are first demonstrated through realisations of the streamwise velocity fields taken at the plane of symmetry of the leaflets (cf. $z = 0$ plane in figure 2). This plane cuts through the leaflets at their maximum chord length and is expected to exhibit the strongest ILEV instabilities, as it corresponds to the largest chord-to-thickness ratio. Three snapshots of the streamwise velocity are shown in figure 4. Various flow features are present. Laminar flow structures similar to Burgers vortices are first observed in the wake of the leaflets. Second, a complex form of shear-layer instabilities is observed in the sinus cavities. This instability only interacts with flow structures in the bulk flow near the centreline after the breakdown in that region has already started. Third, ILEV instabilities are observed downstream of the leading edges of both leaflets, and on their inner surfaces. We note that this latter instability mechanism creates strong flow disturbances which are convected downstream and interact with the other organised wake structures. The interaction of the disturbances created by the ILEV instability mechanism with the wake structures initiates the transition to turbulence in the wake (see the area within the dashed circle in figure 4). Finally, Falkner–Skan boundary layers on the outer sides of the leaflets seem to remain stable in the valve model.

Figure 5 shows the Lagrangian coherent structures around one valve leaflet. The flow field is taken at the peak flow $t = 200$ ms. Four stages of the flow instability are marked
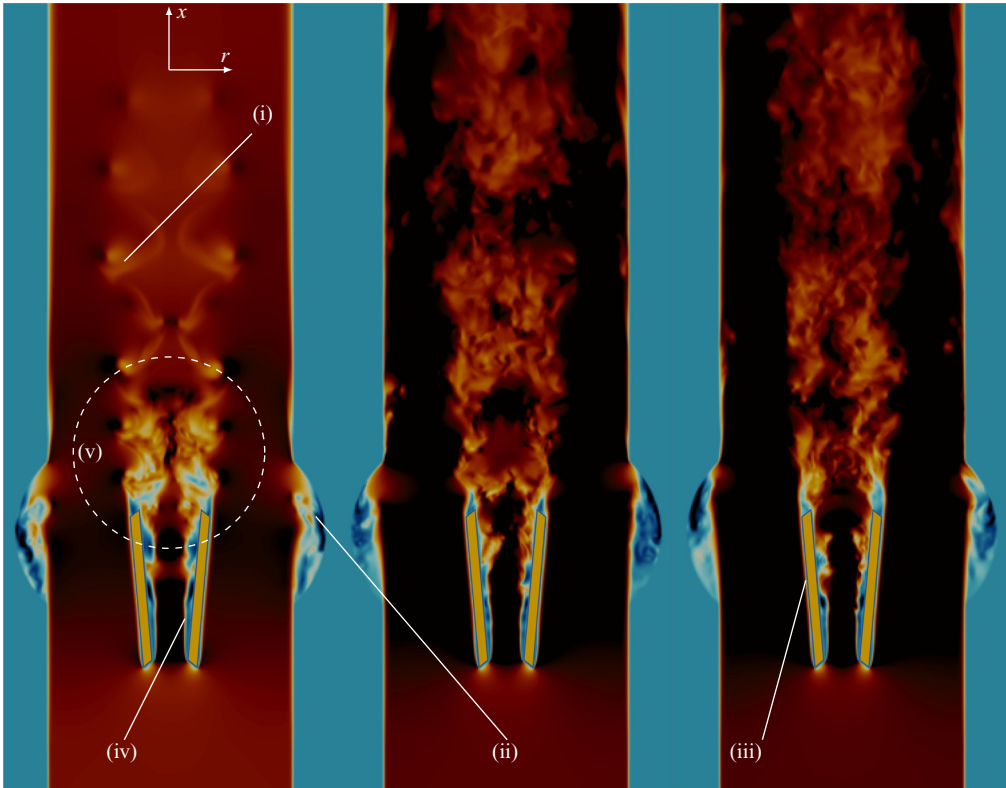
Figure 4. Evolution of the streamwise velocity for the subset of flow field corresponding to the $z = 0$ plane. This plane cuts through the leaflets at their axis of symmetry. Snapshots, from left to right, are taken at $t = 60$, 96 and 132 ms through the acceleration waveform (cf. figure 3). Dark red and dark blue regions show maximum and minimum velocities. Observed flow instabilities include, (i) laminar Burgers-like structures straining in the wake, (ii) 3-D instability in the cavities, (iii) stable Falkner–Skan-type boundary layers with favourable pressure gradients on the outer side of the valve leaflets, (iv) unstable ILEV on the inner sides of the leaflets and (v) nonlinear breakdown in the wake due to an interaction of the instabilities induced by the ILEV with the Burgers vortices in the wake.

with labels LS, PR, SI and TWB, which stand for 'laminar separation', 'primary rolls', 'secondary instabilities' and 'turbulent wake breakdown', respectively. LS corresponds to the shear layer which separates at the leading edge (the laminar part of ILEV) and is inherently uniform in the spanwise direction. This verifies the planar assumption that was used for adopting the 2-D submodel in Zolfaghari & Obrist (2019). It is further quantified here using velocity profiles in the central orifice and over the LS zone (figure 6), which show only small spanwise variations. PR marks the relatively narrow zone where primary instabilities appear on the separated shear layer. The resulting vortex seems to consist of essentially 2-D spanwise rolls. The SI zone shows the area where the primary rolls appearing on the ILEV undergo a secondary instability, triggering a predominantly 3-D dynamics. TWB shows the area where ILEV instabilities interact with the wake structures and create a turbulent state. We will focus on this ILEV instability and on designing possible control strategies to eliminate or attenuate this instability. Ideally, suppressing the primary instability mechanism would result in a laminar flow over the leaflet, and thereby reduce turbulence in the wake area. This was shown using a 2-D control case
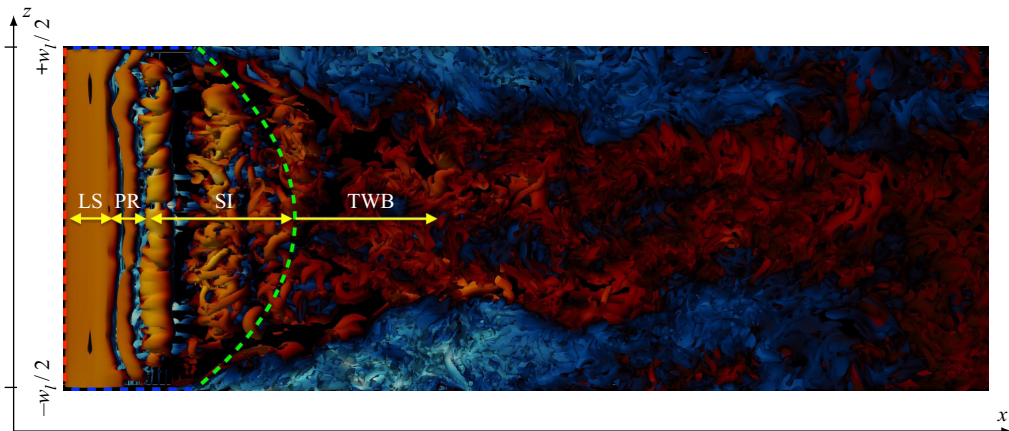
Figure 5. Iso-surfaces of $\lambda_2 = -0.01$ coloured by the streamwise velocity, for a cuboid subset of the flow field encompassing one leaflet in the central orifice area ($2r_h \leq r \leq 0$). Light yellow and light blue regions show maximum and minimum streamwise velocities, respectively. The red dashed line shows the leading edge, and the green dashed line shows the trailing edge. Four zones of flow instability are marked in the streamwise direction. LS denotes the laminar separation zone, which corresponds to a shear layer that is inherently uniform in the spanwise direction. PR shows the narrow extent over which primary rolls appear as a result of a primary ILEV instability. SI marks the approximate interval where primary rolls undergo a secondary instability and become rapidly three-dimensional. TWB shows the turbulent wake breakdown area, where ILEV instabilities interact with leaflet wake structures, causing a turbulent wake.
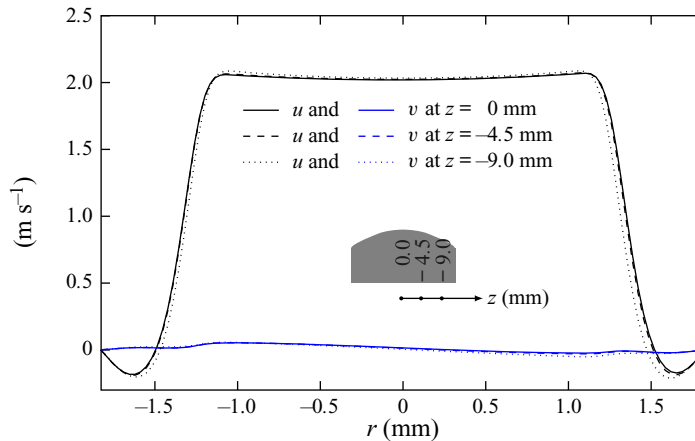

Figure 6. Small spanwise variations in velocity profiles inside the laminar extent of ILEV. Streamwise (black) and cross-stream (blue) velocity profiles are shown for three different spanwise locations $z = 0$ mm, $z = -4.5$ mm and $z = -9$ mm at $t = 72$ ms.

by Zolfaghari & Obrist (2019). Here, we verify this effect in the 3-D model. We modify the leaflets' leading edges in the $z = 0$ plane the same way as in Zolfaghari & Obrist (2019), and apply this modification homogeneously in the spanwise direction. Figure 7 shows that the control case results in a significantly lower oscillations in the wake flow. The cross-section profiles on the right side of this figure show that the elimination of ILEV has resulted in no oscillations in the central orifice.
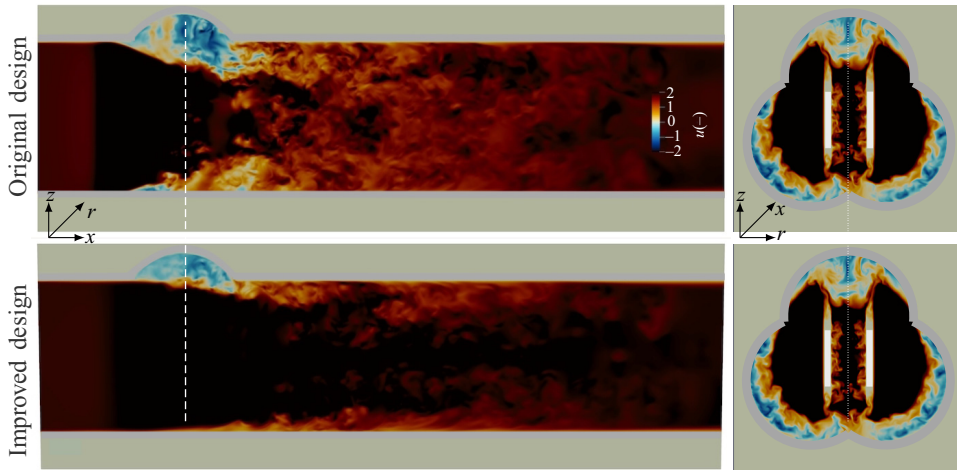
936 A41-10

Figure 7. Effect of ILEV instability on the wake turbulence: streamwise velocity on the $r = 0$ plane (left panels, which correspond to the dotted line on the right panels) and $x = 0$ plane (right panels, which correspond to the dashed line on the left panels) at $t = 84$ ms are shown for the original BMHV design (top) and for the modified leaflet design (bottom). Significantly less wake oscillations are seen for the control case. The cross-sections in the right panels show no oscillatory flow in the central orifice for the control case.

3. Modal linear instability

3.1. *Two-dimensional modal formulation for temporal instability*

We investigate the global linear temporal stability of the time-averaged velocity profiles in the ILEV, as described in Zolfaghari & Obrist (2019). To avoid issues of intractability of the associated eigenvalue problem, we focus on a subdomain covering the extent of the mean 2-D ILEV profile near one leaflet (figure 8). The mean ILEV flow is generated using the same 2-D DNS set-up presented in Zolfaghari & Obrist (2019). Accordingly, the local (ξ, η)-coordinate system described there is used here as well. Briefly recalling relevant details, ξ denotes the streamwise axis with the origin at the leading edge of the leaflets, and η represents the cross-stream axis which originates from the centreline and spans the space between the two leaflets. The η-axis then intersects the upper leaflet at $\eta^*(\xi)$ and the lower leaflet at $-\eta^*(\xi)$.

3.1.1. *Governing equations*

Decomposing the flow field at the leading edge $\tilde{\boldsymbol{q}} = (\tilde{\boldsymbol{u}}, \tilde{p})$ into a mean flow $\tilde{\boldsymbol{Q}} = (\tilde{\boldsymbol{U}}, \tilde{P})$ and a perturbation $\tilde{\boldsymbol{q}}'$ ($\tilde{\boldsymbol{q}} = \tilde{\boldsymbol{Q}} + \tilde{\boldsymbol{q}}'$; $\|\tilde{\boldsymbol{q}}'\| \ll \|\tilde{\boldsymbol{Q}}\|$) and substituting into the Navier–Stokes equations leads to the linearised Navier–Stokes equations which read

$$\partial_t \tilde{\boldsymbol{u}}' + \tilde{\boldsymbol{u}}' \cdot \nabla \tilde{\boldsymbol{U}} + \tilde{\boldsymbol{U}} \cdot \nabla \tilde{\boldsymbol{u}}' = -\nabla \tilde{p}' + \frac{1}{Re_*} \nabla^2 \tilde{\boldsymbol{u}}'; \quad \nabla \cdot \tilde{\boldsymbol{u}}' = 0. \tag{3.1a,b}$$

Here, $\tilde{\boldsymbol{U}}$ denotes the 2-D time-averaged flow field obtained as

$$\tilde{\boldsymbol{U}}(\xi, \eta) = \frac{1}{\tilde{T}} \int_{t_0}^{t_0 + \tilde{T}} \frac{\tilde{\boldsymbol{u}}(\xi, \eta, t)}{U_{max, \xi=0}(t)} \mathrm{d}t. \tag{3.2}$$

The Reynolds number Re_* is based on the maximum streamwise velocity at the leading edge ($U_{max, \xi=0}$) as the reference velocity and the distance between the leaflets at the
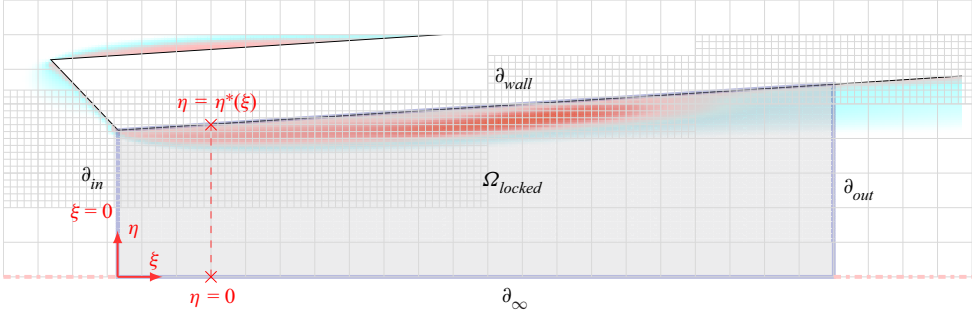
Figure 8. The local subdomain used for the global stability analysis. The grey lines show the background grid $\tilde{\mathcal{G}}$. The true spatial resolution is three times higher than the finer grid patches illustrated near the leaflet boundary. The shaded subdomain represents the grid subset $\mathcal{W}$, for which the global matrices are formed. The grid points near the boundary (labelled as ∂_{wall}) are treated by the sharp-interface immersed boundary method. The local coordinate system (ξ, η) used for the global instability analysis is also given. The origin of the streamwise axis ξ is located at the leaflet's leading edge. The cross-stream axis η extends from the centreline ($\eta = 0$) to the leaflet surface ($\eta = \eta^*(\xi)$) at each streamwise location ξ (see red dashed line).

leading edge ($\eta_0^* = \eta^*(\xi = 0)$) as the reference length. We have

$$Re_* = \frac{\overline{U_{max,\xi=0}}\eta_0^*}{\nu}, \tag{3.3}$$

where

$$\overline{U_{max,\xi=0}} = \frac{1}{\tilde{T}} \int_{t_0}^{t_0+\tilde{T}} U_{max,\xi=0}(t)\, dt. \tag{3.4}$$

Introducing a global mode ansatz of the form $\tilde{q}'(\boldsymbol{x}, t) = \hat{q}(\boldsymbol{x})\, e^{-i\tilde{\beta}t}$, where $\boldsymbol{x}$ and t denote the 2-D spatial coordinates and time, into the LNSE (3.1a,b) yields a system of partial differential equations (PDEs)

$$\begin{bmatrix} \mathcal{L}\{\tilde{\boldsymbol{U}}; Re_*\} + \tilde{U}_\xi & \tilde{U}_\eta & \mathcal{D}_\xi \\ \tilde{V}_\xi & \mathcal{L}\{\tilde{\boldsymbol{U}}; Re_*\} & \mathcal{D}_\eta \\ \mathcal{D}_\xi & \mathcal{D}_\eta & 0 \end{bmatrix} \begin{bmatrix} \hat{u} \\ \hat{v} \\ \hat{p} \end{bmatrix} = i\tilde{\beta} \begin{bmatrix} 1 & 0 & 0 \\ 0 & 1 & 0 \\ 0 & 0 & 0 \end{bmatrix} \begin{bmatrix} \hat{u} \\ \hat{v} \\ \hat{p} \end{bmatrix} \tag{3.5}$$

where $\mathcal{L}\{\tilde{\boldsymbol{U}}; Re_*\} = \tilde{U}\mathcal{D}_\xi + \tilde{V}\mathcal{D}_\eta - 1/Re_*(\mathcal{D}_{\xi\xi} + \mathcal{D}_{\eta\eta})$, and $\hat{q} = (\hat{\boldsymbol{u}}, \hat{p})$ with the velocity vector $\hat{\boldsymbol{u}} = (\hat{u}, \hat{v})$. In the above expression $\mathcal{D}_\xi$ and $\mathcal{D}_{\xi\xi}$ denote the first and second derivatives with respect to the ξ-direction, respectively.

Temporal global modes with $\text{Im}\{\tilde{\beta}\} > 0$ are sought. To this end, we discretise (3.5) using second-order finite-differences with $n_p = 123\,71$ grid points. This results in a complex generalised eigenvalue problem of the form

$$\boldsymbol{A}_{3n_p \times 3n_p}(Re_*, \tilde{\boldsymbol{U}})\hat{\boldsymbol{q}}_{3n_p \times 1} = i\tilde{\beta}\boldsymbol{B}_{3n_p \times 3n_p}\hat{\boldsymbol{q}}_{3n_p \times 1}, \tag{3.6}$$

where $\hat{\boldsymbol{q}}$ is the discretised form of $\hat{q}$.

3.1.2. *Integration of the immersed boundaries*

The sharp-interface immersed boundary method (Mittal *et al.* 2008) is used to integrate the boundary conditions associated with the leaflet walls into the matrices $\boldsymbol{A}$ and $\boldsymbol{B}$ (see (3.6)). The workflow of labelling the grid points according to their position with respect

936 A41-12

to the boundaries is demonstrated in algorithm 1. Compatibility boundary conditions for pressure are imposed on the domain's inlet and outlet as well as on the solid walls. These conditions, in general, read

$$\nabla \tilde{p}' = -\tilde{\boldsymbol{U}} \cdot \nabla \tilde{\boldsymbol{u}}' + \frac{1}{Re_*} \nabla^2 \tilde{\boldsymbol{u}}'. \tag{3.7}$$

On the leaflet walls, this condition simplifies since $\tilde{\boldsymbol{U}} = \boldsymbol{0}$, and (3.7) reduces to

$$\nabla \tilde{p}' = \frac{1}{Re_*} \nabla^2 \tilde{\boldsymbol{u}}'. \tag{3.8}$$

The compatibility boundary conditions, together with zero-disturbance Dirichlet boundary conditions for the velocity vector given by

$$\tilde{\boldsymbol{u}}'(\boldsymbol{x}, t) = 0, \quad \boldsymbol{x} \in \partial_{in} \cup \partial_{walls} \cup \partial_{out} \cup \partial_\infty, \tag{3.9}$$

are discretised and integrated into the matrices $\boldsymbol{A}$ and $\boldsymbol{B}$. To save computational time, and owing to the symmetry of the velocity profiles, only half of the profile is considered, which is results in a symmetry boundary condition at $\tilde{\eta} = 0$.

Algorithm 1: Two-dimensional global instability solver with immersed boundaries

---

Result: Subset of eigenvalues and eigenfunctions $\mathcal{S} = \{(\beta_s, \hat{\boldsymbol{q}}_s) | 1 \le s \le N\}$.
Data: Time-resolved DNS flow field data $\tilde{\boldsymbol{q}}(t) = (\tilde{\boldsymbol{u}}, \tilde{p})$ on grid $\tilde{\mathcal{G}}$.
1. Compute the time-averaged velocity field $\tilde{\boldsymbol{U}}$;
2. Create a subset of $\tilde{\mathcal{G}}$ called $\mathcal{G}_{m \times n}$ with favourable resolution and encompassing the ILEV domain ;
3. Cut off the solid subset of the $\mathcal{G}_{m \times n}$:
for $\boldsymbol{x} \in \mathcal{G}_{m \times n}$ **do**
    if *fluid* **then**
        append $\boldsymbol{x}$ to the work grid $\mathcal{W}$;
        label $\boldsymbol{x}$ as $\underbrace{\Omega_{locked}}_{\text{inner point}}$, $\underbrace{\partial_{in}}_{\text{inflow}}$, $\underbrace{\partial_{out}}_{\text{outflow}}$, $\underbrace{\partial_{wall}}_{\text{on leaflet}}$, $\underbrace{\partial_\infty}_{\text{centreline}}$;
    end
end
4. Form $\boldsymbol{A}$ and $\boldsymbol{B}$:
for *each point* $\boldsymbol{x} \in \mathcal{W}$ **do**
    get label of $\boldsymbol{x}$;
    calculate $\tilde{U}_\xi, \tilde{U}_\eta, \tilde{V}_\xi, \tilde{V}_\eta$ on $\mathcal{G}_{m \times n}$;
    form operators $\mathscr{D}_\xi, \mathscr{D}_{\xi\xi}, \mathscr{D}_\eta, \mathscr{D}_{\eta\eta}$ and
      $\mathscr{L}\{\tilde{\boldsymbol{U}}; Re_*\} = \tilde{U} \mathscr{D}_\xi + \tilde{V} \mathscr{D}_\eta + 1/Re_*(\mathscr{D}_{\xi\xi} + \mathscr{D}_{\eta\eta})$;
    fill up rows $3j - i$, $i = 1, 2, 3$ and $1 \le j \le size(\mathcal{W})$ in $\boldsymbol{A}$ and $\boldsymbol{B}$;
end
5. Solve the eigenvalue problem $\boldsymbol{A}\hat{\boldsymbol{q}} = i\tilde{\beta}\boldsymbol{B}\hat{\boldsymbol{q}}$;
6. Retrieve eigenvectors on $\tilde{\mathcal{G}}$ by an inverse mapping $\mathcal{W} \to \tilde{\mathcal{G}}$.

Figure 9 shows the real part of the streamwise velocity component of the two zero-frequency global eigenmodes with positive temporal growth rates. Mode A, which
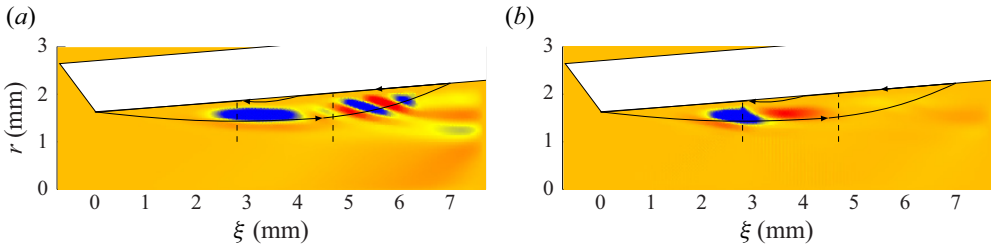
Figure 9. Global modes (*a*) A and (*b*) B, visualised by the real part of the streamwise velocity component. Dashed lines mark the extent of the local absolute instability. Approximate separation streamlines for the mean flow are drawn as solid black lines. Dark red and dark blue colours indicate the colour map extrema.

has a higher growth rate, has a similar spatial structure than the one found for X-junction flow (Lashgari *et al.* 2014), stretching from the separation point to the trailing end of the wave-maker zone. This could be related to similarities in the two base flows: both include flow separation downstream of a sharp edge. Yet, our mode presents more waviness past the wave maker, which includes the area where the separated shear layer reattaches. This waviness may be attributed to the strong fluctuations that are observed over the reattachment zone of ILEV structures, which were also reported by Cherry, Hillier & Latour (1984). Mode B, on the other hand, is more concentrated near the leading edge of the wave-maker zone. It slowly emerges on the separated shear layer nearly two thickness lengths downstream of the leading edge, and vanishes towards the reattachment zone. Provided this mode is present where the shear layer has the highest reverse-to-forward flow ratio, it projects the dynamics of the shear layer seemingly uninfluenced by the presence of the wall. This is in contrast to mode A, where oscillatory effects can be observed at locations where this latter ratio is low. In line with this, mode A includes a wavy structure that is extended to the outflow boundary, before it is affected by the homogeneous Dirichlet boundary conditions there. We will show in Appendix A that the structure of this mode and mode B (as well as their associated eigenvalues) do not change when the outflow boundary is extended further downstream.

3.2. *Structural sensitivity of the linear global modes*

3.2.1. *Adjoint modal formulation*

For investigating the sensitivity of the global modes characteristics (e.g. their growth rates) to the underlying flow, adjoints of the global modes are studied. For the pairs $(\tilde{\boldsymbol{u}}', \tilde{p}')$ and $(\tilde{\boldsymbol{u}}'^{,\dagger}, \tilde{p}'^{,\dagger})$ the following Lagrange identity holds as:

$$[\mathscr{P} \cdot \tilde{\boldsymbol{u}}'^{,\dagger} + \nabla \cdot \tilde{\boldsymbol{u}}' \tilde{p}'^{,\dagger}] + [\tilde{\boldsymbol{u}}' \cdot \mathscr{P}^{\dagger} + \nabla \cdot \tilde{\boldsymbol{u}}'^{,\dagger} \tilde{p}'] = \partial_t (\tilde{\boldsymbol{u}}' \cdot \tilde{\boldsymbol{u}}'^{,\dagger}) + \nabla \cdot \boldsymbol{M}^{\dagger}, \qquad (3.10)$$

where

$$\mathscr{P}\{\tilde{\boldsymbol{u}}', \tilde{p}', \tilde{\boldsymbol{U}}, Re_*\} = \partial_t \tilde{\boldsymbol{u}}' + \tilde{\boldsymbol{U}} \cdot \nabla \tilde{\boldsymbol{u}}' + \tilde{\boldsymbol{u}}' \cdot \nabla \tilde{\boldsymbol{U}} + \nabla \tilde{p}' - \frac{1}{Re_*} \nabla^2 \tilde{\boldsymbol{u}}'^{,\dagger}, \qquad (3.11)$$

and

$$\mathscr{P}^{\dagger}\{\tilde{\boldsymbol{u}}'^{,\dagger}, \tilde{p}'^{,\dagger}, \tilde{\boldsymbol{U}}, Re_*\} = \partial_t \tilde{\boldsymbol{u}}'^{,\dagger} + \tilde{\boldsymbol{U}} \cdot \nabla \tilde{\boldsymbol{u}}'^{,\dagger} - \tilde{\boldsymbol{u}}'^{,\dagger} \cdot (\nabla \tilde{\boldsymbol{U}})^{\mathrm{T}} + \nabla \tilde{p}'^{,\dagger} + \frac{1}{Re_*} \nabla^2 \tilde{\boldsymbol{u}}'^{,\dagger}. \qquad (3.12)$$

Here, $\boldsymbol{M}^\dagger$ is the bilinear concomitant defined as

$$\boldsymbol{M}^\dagger = \tilde{\boldsymbol{U}}(\tilde{\boldsymbol{u}}' \cdot \tilde{\boldsymbol{u}}'^{,\dagger}) + \frac{1}{Re_*}(\nabla \tilde{\boldsymbol{u}}'^{,\dagger} \cdot \tilde{\boldsymbol{u}}' - \nabla \tilde{\boldsymbol{u}}' \cdot \tilde{\boldsymbol{u}}'^{,\dagger}) + \tilde{p}'^{,\dagger}\tilde{\boldsymbol{u}}' + \tilde{p}'\tilde{\boldsymbol{u}}'^{,\dagger}. \tag{3.13}$$

Integrating the Lagrange identity over the entire domain and over the chosen time horizon and using the divergence theorem for the last term, we obtain the adjoint LNSE in the form

$$\mathscr{P}^\dagger\{\tilde{\boldsymbol{u}}'^{,\dagger}, \tilde{p}'^{,\dagger}, \tilde{\boldsymbol{U}}, Re_*\} = 0; \quad \nabla \cdot \tilde{\boldsymbol{u}}'^{,\dagger} = 0. \tag{3.14a,b}$$

Fourier transformation of (3.10) using the ansatz $\tilde{\boldsymbol{q}}'^{,\dagger}(\boldsymbol{x}, t) = \hat{\boldsymbol{q}}^\dagger(\boldsymbol{x})\,\mathrm{e}^{-\mathrm{i}\tilde{\beta}^\dagger t}$, where $\boldsymbol{x}$ and t are the 2-D spatial coordinates and time, gives the coupled form of the adjoint LNSE

$$\begin{bmatrix} \mathscr{L}^\dagger\{\tilde{\boldsymbol{U}}; Re_*\} - \partial_\xi \tilde{U} & -\partial_\xi \tilde{V} & \mathscr{D}_\xi \\ -\partial_\eta \tilde{U} & \mathscr{L}^\dagger\{\tilde{\boldsymbol{U}}; Re_*\} - \partial_\eta \tilde{V} & \mathscr{D}_\eta \\ \mathscr{D}_\xi & \mathscr{D}_\eta & 0 \end{bmatrix} \begin{bmatrix} \hat{u}^\dagger \\ \hat{v}^\dagger \\ \hat{p}^\dagger \end{bmatrix} = \mathrm{i}\tilde{\beta}^\dagger \begin{bmatrix} 1 & 0 & 0 \\ 0 & 1 & 0 \\ 0 & 0 & 0 \end{bmatrix} \begin{bmatrix} \hat{u}^\dagger \\ \hat{v}^\dagger \\ \hat{p}^\dagger \end{bmatrix}, \tag{3.15}$$

where $\mathscr{L}^\dagger\{\tilde{\boldsymbol{U}}; Re_*\} = \tilde{U}\mathscr{D}_\xi + \tilde{V}\mathscr{D}_\eta + Re_*^{-1}(\mathscr{D}_{\xi\xi} + \mathscr{D}_{\eta\eta})$, $\hat{\boldsymbol{q}}^\dagger = (\hat{\boldsymbol{u}}^\dagger, \hat{p}^\dagger)$ and $\hat{\boldsymbol{u}}^\dagger = (\hat{u}^\dagger, \hat{v}^\dagger)$. The operators $\mathscr{D}_\xi$ and $\mathscr{D}_{\xi\xi}$ denote the first and second derivatives with respect to ξ, respectively. Discretisation yields the generalised eigenvalue problem

$$\boldsymbol{A}^\dagger_{3n_p \times 3n_p}(\tilde{\boldsymbol{U}}, Re_*)\hat{\boldsymbol{q}}^\dagger_{3n_p \times 1} = \mathrm{i}\tilde{\beta}^\dagger \boldsymbol{B}^\dagger_{3n_p \times 3n_p}(\tilde{\boldsymbol{U}}, Re_*)\hat{\boldsymbol{q}}^\dagger_{3n_p \times 1}, \tag{3.16}$$

where $\hat{\boldsymbol{q}}^\dagger$ is the discretised form of adjoint state vector. Homogeneous Dirichlet boundary conditions for the adjoint velocity disturbances $\tilde{\boldsymbol{u}}'^{,\dagger}$ are applied, together with compatibility boundary condition for the adjoint pressure disturbance $\tilde{p}'^{,\dagger}$. The compatibility boundary conditions for $\tilde{p}'^{,\dagger}$ prove to be the proper choice for the domain's inflow and outflow. To obtain the adjoint compatibility boundary conditions, we first substitute this condition for the direct problem (3.7) into the momentum component of the direct linearised Navier–Stokes equations (3.1a,b). This yields

$$\partial_t \tilde{\boldsymbol{u}}' + \tilde{\boldsymbol{u}}' \cdot \nabla \tilde{\boldsymbol{U}} = 0, \tag{3.17}$$

which, in the adjoint form, becomes

$$\partial_t \tilde{\boldsymbol{u}}'^{,\dagger} + \tilde{\boldsymbol{U}} \cdot \nabla \tilde{\boldsymbol{u}}'^{,\dagger} = 0. \tag{3.18}$$

Equation (3.18) is incorporated into $\boldsymbol{A}^\dagger$ and $\boldsymbol{B}^\dagger$ at the inflow, centreline, and outflow locations, where $\tilde{\boldsymbol{U}} \neq \boldsymbol{0}$.

Figure 10 shows the adjoint global modes corresponding to the direct global modes A and B. The adjoint modes can be used to quantify the sensitivity of the global direct modes to external forcing (Giannetti & Luchini 2007). We use both direct and adjoint modes for constructing the structural sensitivity tensor which can be used to guide the stabilisation of these modes.

3.2.2. *Structural sensitivity to a local feedback source*

We follow the localised momentum feedback approach pioneered by Hill (1992) and Giannetti & Luchini (2007). We perturb the momentum equation of the LNSE, after
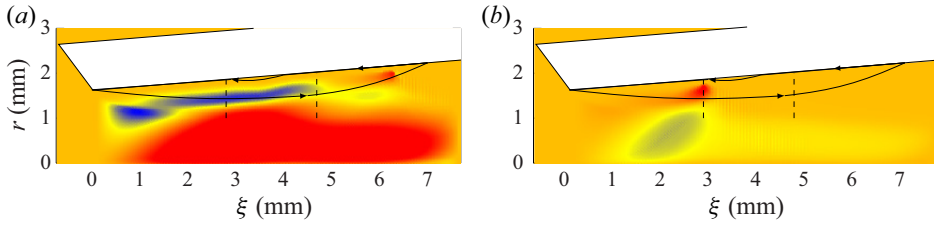
Figure 10. Adjoint global modes (*a*) A and (*b*) B, visualised by the streamwise velocity component. Dashed lines mark the extent of the local absolute instability. Approximate separation streamlines for the mean flow are drawn as solid black lines. Dark red and dark blue colours indicate the colour map extrema. Larger magnitudes correspond to higher sensitivities of the global modes to the underlying flow.

Fourier decomposition in time, by the linear operator $\delta\mathcal{M}$

$$\left.\begin{aligned} \tilde{\beta}'\hat{\boldsymbol{u}}' + \mathcal{L}^+\{\tilde{\boldsymbol{U}}, Re_*\}\hat{\boldsymbol{u}}' + \nabla\hat{p}' = \delta\mathcal{M}(\hat{\boldsymbol{u}}', \hat{p}') \\ \nabla \cdot \hat{\boldsymbol{u}}' = 0, \end{aligned}\right\}, \tag{3.19}$$

where the $\mathcal{L}^+$ operator is given as

$$\mathcal{L}^+\{\tilde{\boldsymbol{U}}, Re_*\}\hat{\boldsymbol{u}}' = \hat{\boldsymbol{u}}' \cdot \nabla\tilde{\boldsymbol{U}} + \tilde{\boldsymbol{U}} \cdot \nabla\hat{\boldsymbol{u}}' - \frac{1}{Re_*}\nabla^2\hat{\boldsymbol{u}}'. \tag{3.20}$$

Given the eigenvalue drift $\delta\tilde{\beta}$ and the perturbation eigenmode $(\delta\hat{\boldsymbol{u}}, \delta\hat{p})$, where $\hat{\boldsymbol{u}}' = \hat{\boldsymbol{u}} + \delta\hat{\boldsymbol{u}}, \hat{p}' = \hat{p} + \delta\hat{p}$ and $\tilde{\beta}' = \tilde{\beta} + \delta\tilde{\beta}$, we arrive at

$$\left.\begin{aligned} \tilde{\beta}\delta\hat{\boldsymbol{u}} + \mathcal{L}^+\{\tilde{\boldsymbol{U}}, Re_*\}\delta\hat{\boldsymbol{u}} + \nabla\delta\hat{p} = -\delta\tilde{\beta}\hat{\boldsymbol{u}} + \delta\mathcal{M}(\hat{\boldsymbol{u}}, \hat{p}) \\ \nabla \cdot \delta\hat{\boldsymbol{u}} = 0, \end{aligned}\right\} \tag{3.21}$$

using the Lagrange identity (similar to (3.10)) for $(\delta\hat{\boldsymbol{u}}, \delta\hat{p})$ and $(\hat{\boldsymbol{u}}^\dagger, \hat{p}^\dagger)$. Taking $\delta\mathcal{M} = \boldsymbol{K}\hat{\boldsymbol{u}}\delta_{\boldsymbol{D}}(\xi - \xi_+, \eta - \eta_+)$ and integrating over the entire computational domain, one obtains

$$\delta\tilde{\beta} = \frac{\langle\hat{\boldsymbol{u}}^\dagger \cdot \delta\mathcal{M}\rangle}{\langle\hat{\boldsymbol{u}} \cdot \hat{\boldsymbol{u}}^\dagger\rangle} = \frac{\langle\hat{\boldsymbol{u}}^\dagger \cdot \boldsymbol{K}\hat{\boldsymbol{u}}\delta_{\boldsymbol{D}}(\xi - \xi_+, \eta - \eta_+)\rangle}{\langle\hat{\boldsymbol{u}} \cdot \hat{\boldsymbol{u}}^\dagger\rangle} = \frac{\kappa_0\hat{\boldsymbol{u}}(\xi_+, \eta_+)\hat{\boldsymbol{u}}^\dagger(\xi_+, \eta_+)}{\langle\hat{\boldsymbol{u}} \cdot \hat{\boldsymbol{u}}^\dagger\rangle}. \tag{3.22}$$

In the above formulation, $\delta_{\boldsymbol{D}}$ is the Dirac delta function, $\langle\cdot\rangle$ is the integral over the computational domain and $\boldsymbol{K}$ and $\kappa_0 = \boldsymbol{K}(\xi_+, \eta_+)$ indicate the strength of the momentum feedback on the entire domain and at point (ξ_+, η_+), respectively. It follows that the response of each component of momentum feedback on the growth rate and frequency of the global modes can be realised by assessing the real and imaginary parts of the sensitivity tensor $\boldsymbol{S} = \hat{\boldsymbol{u}} \otimes \hat{\boldsymbol{u}}^\dagger$, which consists of the dyadic product of the direct and adjoint velocity modes. The imaginary part of the components of $\boldsymbol{S}$ measure the sensitivity of the global mode with respect to the growth rate, while the real part determines the sensitivity with respect to the frequency. Here, we focus on the imaginary part, as we are interested in stabilisation of the modes, hoping to eliminate the vortex shedding between and downstream of the leaflets of the BMHV.

The components of the sensitivity tensor associated with modes A and B are given in figures 11 and 12. For mode A, the highest sensitivities are generally concentrated in the wave-maker zone. This is not surprising as a local absolute instability is defined by an instability with infinite impulse response at a fixed location. A feedback, if sufficiently small to preserve the instability characteristics of the base flow, could be seen in extreme cases as an input, which will be maximally amplified in the wave-maker zone. In terms of
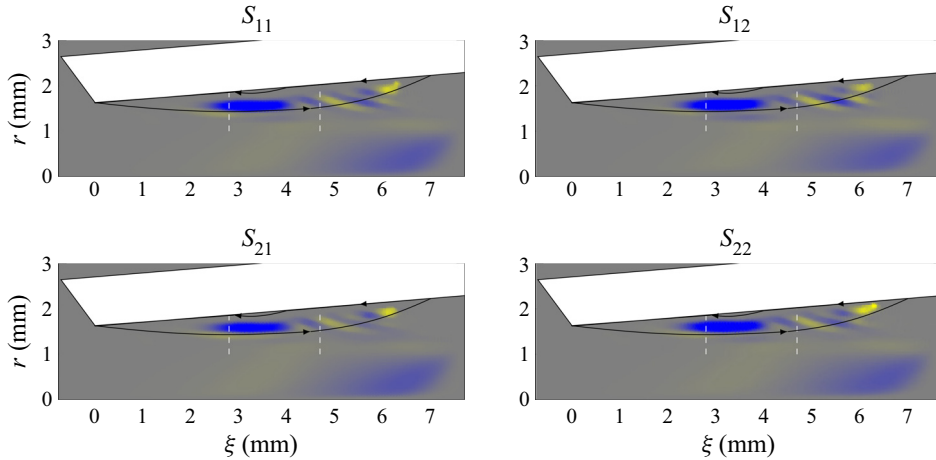
936 A41-16

Figure 11. Components of the sensitivity tensor **S** for mode A. Yellow areas denote the maximum, blue areas denote the minimum sensitivity. The domain between the dashed white lines is locally absolutely unstable.
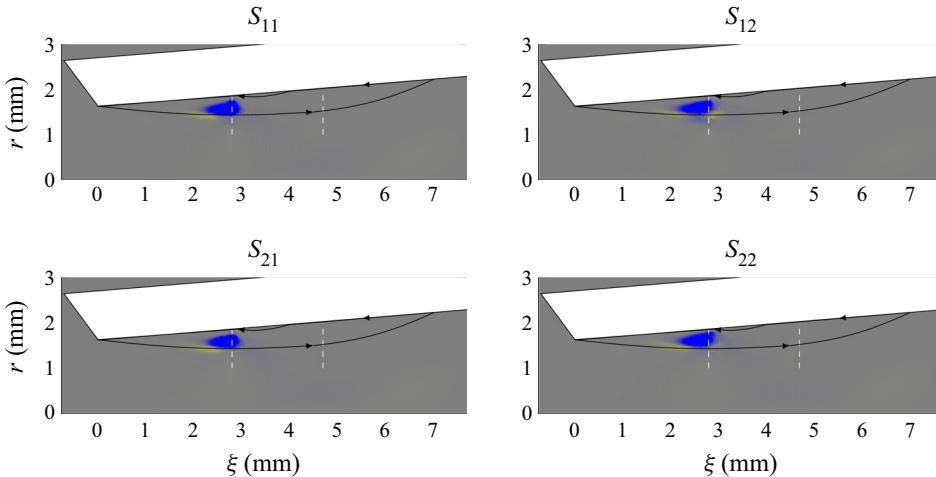

Figure 12. Components of the sensitivity tensor **S** for mode B. Yellow areas denote the maximum, blue areas denote the minimum sensitivity. The domain between the dashed white lines is locally absolutely unstable (wave-maker region).

different components of sensitivity, $S_{12} = \hat{u}\hat{v}^{\dagger}$ appears to have a slightly higher magnitude than other components. This implies that, within a linear regime, a forcing in the cross-stream direction will trigger the largest response in the streamwise component of the direct mode. This could be explained by further investigating the characteristics of the base flow, such as the properties of the rate of strain tensor, but such an analysis will be postponed to a future effort. For mode B, the maximum structural sensitivity occurs upstream and almost completely outside the wave-maker zone. This observation signals a large influence of the base flow on the dynamics of this shear-layer mode, possibly through a feedback mechanism supported by recirculation.

3.2.3. *Passive control based on localised feedback*

Motivated by the original experimental work of Strykowski & Sreenivasan (1990) and the follow-up theoretical study of Hill (1992) who tried to suppress the first instability of cylinder wake flow at $Re \approx 50$ by introducing localised roughness elements into the

system, we use this technique to try to suppress the ILEV instabilities in the BMHVs. Several differences exist between the two cases, the most importantly, the two orders of magnitude larger Reynolds number of the BMHV flow compared with the cylinder wake flow. It is also not clear whether a localised feedback will strengthen, or weaken the instability. Besides, given that more than one global mode is involved, with high structural sensitivities in distinct locations, the likelihood that only one feedback source may eliminate the instability entirely is likely small. It is also important to note that, because the Reynolds number is relatively high in our case, a localised feedback, positioned relatively far from the wall may cause more instability, e.g. via introducing von-Kármán-type vortex streets. Despite these apprehensions, we nonetheless put our findings from the linear structural sensitivity analysis to the test by performing 2-D DNSs. We introduce small feedback sources in the form of small cylinders (far from the wall, for mode A), or in the form of a semicircular bump (close to the wall, for mode B), and perform 2-D DNS using the parameters from Zolfaghari & Obrist (2019). For mode A, we observed that a localised feedback did not seem to improve the flow scenario (not shown). The inserted cylinder near the upstream end of the wave-maker zone created instabilities which evolved into travelling vortices downstream of the feedback source. Given that mode B was not triggered, it induced waviness in the ILEV which interacted with the instabilities created by the cylinder. For mode B, we anticipated a more positive outcome, as this mode has a more localised sensitivity compared with mode A. This localised area is closer to the wall which, due to lower velocities and a smaller surface, generates less drag force on the original base flow. Thus, the base flow characteristics are likely to change less than for mode A. Significant changes in the base flow $\tilde{\boldsymbol{U}}$ may render the structural sensitivity analysis invalid, because the eigenvalue shift $\delta\beta$ based on (3.22) assumes small and thus negligible changes in the base flow. A better outcome is also expected because the area to be triggered lies outside the absolute instability zone. For this reason, the chances of triggering more instabilities by the large impulse response of the wave maker are rather low.

Figure 13 shows the outcome of passive control via local feedback associated with mode B. For the local feedback, two small and equal circular bumps with a radius of $R_c = 0.126$ mm were added on both leaflet surfaces at $\xi_c = 4.95$ and $\eta_c = \pm 1.68$ mm. The positions of these bumps were chosen to be approximately in the centre of the maximum sensitivity area for mode B. It can be observed that with passive control the vorticity production between the leaflets was diminished, but not eliminated. In more detail, as shown using instantaneous vorticity fields, the location where first vortices, forming due to ILEV instabilities, detach into the bulk flow could be moved downstream by nearly one third of a chord length. Thanks to this improvement, the mutual interaction between the vortices, generated by ILEVs and forming on the top and bottom leaflets, was nearly eliminated. In general, even though the ILEV instability could not be fully controlled, this passive control device resulted in a noticeably less chaotic wake flow past the valve. This is further quantified in figure 14 using area-normalised enstrophy defined as

$$E_S(\boldsymbol{\omega}) = \frac{1}{S} \int_S \boldsymbol{\omega} \cdot \boldsymbol{\omega} \, \mathrm{d}S, \tag{3.23}$$

where $\boldsymbol{\omega} = \nabla \times \boldsymbol{u}$ is the vorticity and S indicates the circular area where the integration is performed. Significantly lower enstrophy is found for the control case both within the central orifice and in the wake, which demonstrates the efficacy of the control.
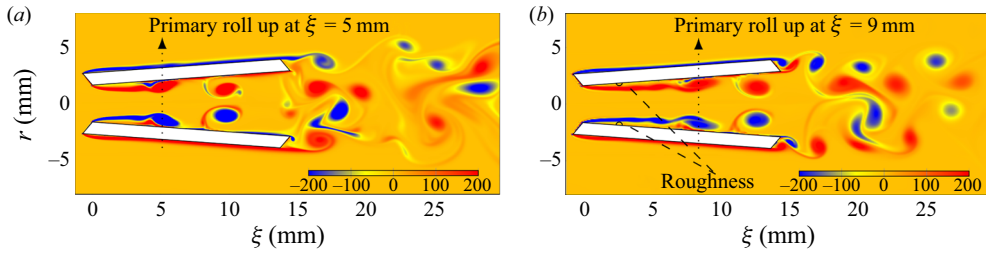
936 A41-18

Figure 13. Instantaneous vorticity for (*a*) baseline ILEV flow and (*b*) ILEV flow with local feedback control corresponding to mode B.
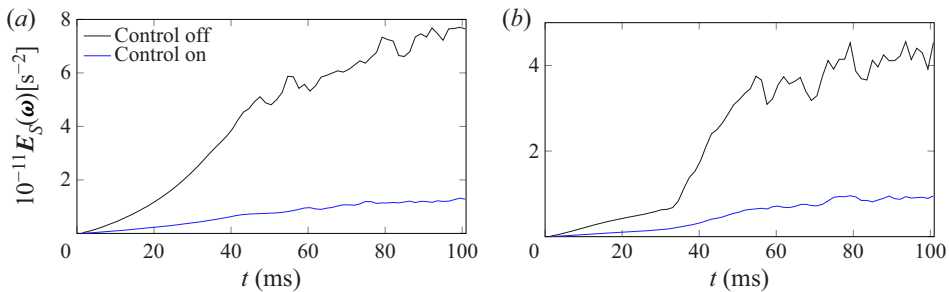

Figure 14. Effect of passive control based on momentum feedback on normalised enstrophy $E_S(\boldsymbol{\omega})$ at ((*a*), in central orifice) 5.76 mm and ((*b*), in the wake) 12.96 mm downstream of the leading edge. The integration area S was a circle of radius 3.6 mm and centred on $r = 0$ mm.

4. Disturbance energy growth analysis

The hydrodynamic stability analyses performed in the previous section and by Zolfaghari & Obrist (2019) were asymptotic and focused on the ILEV zone of the BMHV flow. While this type of analysis is useful for understanding the instability mechanism itself, the influence of the ILEV instability on disturbance energy growth farther from its origin is also worth investigating. Zolfaghari & Obrist (2019) showed by a geometry modification that the ILEV instability plays a key role in the laminar–turbulent transition of the valve wake. Without this modification, it would have been difficult to distinguish between ILEV instabilities and other mechanisms, e.g. the wake instability or driving by the cavities. Ideally, the strongest mechanism contributing to transition in a certain location, such as the wake, should be identified and analysed. In addition, the influence of various mechanisms is mostly time dependent, with the disturbance energy growth at a given location being driven by local mechanisms over shorter times. In the following, we formulate a linear gradient-based approach (Schmid 2007; Schmid, de Pando & Peake 2017) to study the contribution of the ILEV instabilities at arbitrary locations and over given short-time horizons.

4.1. *Direct non-modal formulation*

4.1.1. *Governing equations*

We again consider the incompressible Navier–Stokes equations for a disturbance ($\tilde{\boldsymbol{u}}', \tilde{p}'$) around a global mean flow ($\tilde{\boldsymbol{U}}, \tilde{\boldsymbol{P}}$),

$$\partial_t \tilde{\boldsymbol{u}}' + \tilde{\boldsymbol{u}}' \cdot \nabla \tilde{\boldsymbol{U}} + \tilde{\boldsymbol{U}} \cdot \nabla \tilde{\boldsymbol{u}}' = -\nabla \tilde{p}' + \frac{1}{Re} \nabla^2 \tilde{\boldsymbol{u}}'; \quad \nabla \cdot \tilde{\boldsymbol{u}}' = 0, \tag{4.1a,b}$$
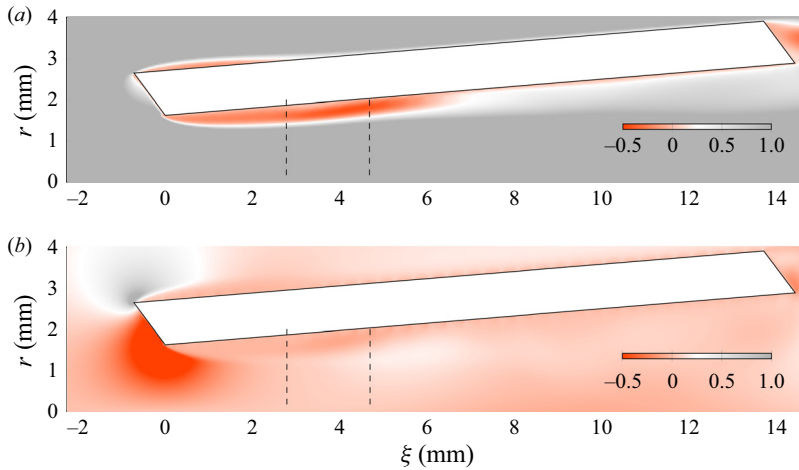
936 A41-19

Figure 15. Time-averaged (*a*) streamwise and (*b*) cross-stream velocity components around the ILEV in the BMHV.

and seek to recover the ILEV instabilities as disturbances superimposed on a mean flow $\tilde{U}$ at each time t. Note that we use a different mean flow for the nonlinear non-modal analysis than for the earlier linear modal approach give in (3.1*a,b*). Here, $\tilde{U}$ is obtained by temporally averaging of the velocity field $\tilde{u}$; no scaling is involved, and the averaging is performed over the entire flow domain. We have

$$\tilde{U}(x, r) = \frac{1}{\tilde{T}} \int_{t_0}^{t_0+\tilde{T}} \tilde{u}(x, r, t)\, dt, \qquad (4.2)$$

which also implies that the statistical averaging is performed over the global (x, r) instead of the local (ξ, η) coordinates. The time-averaged flow field around the ILEV is shown in figure 15.

4.2. *Adjoint equations with focus on arbitrary geometric energy masks*

In order to study the optimal perturbations for maximising energy growth in specific locations within the computational domain (e.g. around the ILEV zone, or in the wake) we formulate the Lagrangian

$$\mathcal{L} = \underbrace{\frac{1}{2} \langle \mathcal{G}\tilde{u}'(\boldsymbol{x}, T) \cdot \mathcal{G}\tilde{u}'(\boldsymbol{x}, T)\rangle}_{\mathcal{J}_{\mathcal{G}}} + \phi \left\{ \frac{1}{2} \langle \tilde{u}'(\boldsymbol{x}, 0) \cdot \tilde{u}'(\boldsymbol{x}, 0)\rangle - E_0 \right\}$$
$$+ \int_0^T \left\langle \tilde{u}'^{,\ddagger} \cdot \{\partial_t \tilde{u}' + \tilde{u}' \cdot \nabla \tilde{U} + \tilde{U} \cdot \nabla \tilde{u}' + \nabla \tilde{p}' - Re^{-1}\nabla^2 \tilde{u}'\}\right\rangle dt + \int_0^T \left\langle \tilde{p}'^{,\ddagger}\nabla \cdot \tilde{u}'\right\rangle dt, \qquad (4.3)$$

where $\mathcal{J}_{\mathcal{G}}$ is an objective equipped with a sharp-interface geometric mask function $\mathcal{G}$: $\Omega \to \Omega_v$, which projects the global flow field onto the subdomain of interest Ω_v. This function is used to focus the optimisation procedure on the disturbance kinetic energy within Ω_v, which is moved over various areas of interest such as the wake and the trailing edge, to inspect the potential role of ILEV instabilities. The pair $(\tilde{u}'^{,\ddagger}, \tilde{p}'^{,\ddagger})$ denotes the

936 A41-20

adjoint of the direct disturbances $(\tilde{\boldsymbol{u}}', \tilde{p}')$, and $\langle \cdot \rangle$ stands for the integral over the entire domain Ω. By using first variations of the Lagrangian with respect to the variables $\tilde{p}'$, $\tilde{\boldsymbol{u}}'$, integration by parts and forming the associated Frechet derivatives (see Appendix B), the adjoint linearised Navier–Stokes equations are found.

For optimality, the Frechet derivative of $\mathcal{L}$ with respect to $\delta\tilde{\boldsymbol{u}}'$, $\delta\tilde{\boldsymbol{u}}'(0)$ and $\delta\tilde{\boldsymbol{u}}'(T)$ must vanish. These constraints yield the following identities:

$$\partial_{\delta\tilde{\boldsymbol{u}}'}\mathcal{L} = 0 \Rightarrow \partial_t\tilde{\boldsymbol{u}}'^{,\ddagger} + \tilde{\boldsymbol{U}} \cdot \boldsymbol{\nabla}\tilde{\boldsymbol{u}}'^{,\ddagger} - \tilde{\boldsymbol{u}}'^{,\ddagger} \cdot (\boldsymbol{\nabla}\tilde{\boldsymbol{U}})^{\mathrm{T}} - \boldsymbol{\nabla}\tilde{p}'^{,\ddagger} + Re^{-1}\nabla^2\tilde{\boldsymbol{u}}'^{,\ddagger} = 0, \quad (4.4)$$

which is the adjoint momentum of the incompressible Navier–Stokes equations,

$$\partial_{\delta\tilde{\boldsymbol{u}}'(\boldsymbol{x},0)}\mathcal{L} = 0 \Rightarrow \phi\tilde{\boldsymbol{u}}'(\boldsymbol{x}, 0) = \tilde{\boldsymbol{u}}'^{,\ddagger}(\boldsymbol{x}, 0), \quad (4.5)$$

which gives the initial condition for the direct problem, and

$$\partial_{\delta\tilde{\boldsymbol{u}}'(\boldsymbol{x},T)}\mathcal{L} = 0 \Rightarrow \mathcal{G}\tilde{\boldsymbol{u}}'(\boldsymbol{x}, T) = -\tilde{\boldsymbol{u}}'^{,\ddagger}(\boldsymbol{x}, T), \quad (4.6)$$

which provides the initial condition for the adjoint problem. Note that the geometric mapping function $\mathcal{G}$, which we introduced in the objective $\mathcal{J}_{\mathcal{G}}$, appears in the terminal condition.

Direct and adjoint fields are then computed via iterative direct–adjoint looping (DAL) simulations. At each iteration of DAL, (i) the direct problem (3.1*a,b*) is integrated forward in time from $t = 0$ to $t = T$; (ii) initial conditions for the adjoint problem (4.6) are set; (iii) the adjoint problem (4.4) is integrated backward in time from $t = T$ to $t = 0$; (iv) initial conditions for the direct problem are updated as follows and the next iteration starts. The initial condition $\tilde{\boldsymbol{u}}'(0)$ is corrected based on a steepest ascent procedure

$$\tilde{\boldsymbol{u}}'(\boldsymbol{x}, 0)^{k+1} = \tilde{\boldsymbol{u}}'(\boldsymbol{x}, 0)^k + \frac{\epsilon_s}{\phi}\partial_{\tilde{\boldsymbol{u}}'(\boldsymbol{x},0)}\mathcal{L} = (1 + \epsilon_s)\tilde{\boldsymbol{u}}'(\boldsymbol{x}, 0)^k - \frac{\epsilon_s}{\phi}\tilde{\boldsymbol{u}}'^{,\ddagger}(\boldsymbol{x}, 0)^k, \quad (4.7)$$

where ϵ_s is a user-specified parameter, while ϕ is updated to enforce

$$\frac{1}{2}\left\langle \tilde{\boldsymbol{u}}'(\boldsymbol{x}, 0)^{k+1} \cdot \tilde{\boldsymbol{u}}'(\boldsymbol{x}, 0)^{k+1} \right\rangle = E_0. \quad (4.8)$$

We validate our implementation by reproducing the transient growth calculations for plane Poiseuille flow at $Re = 3000$. Good agreement is found, which is reported in Appendix C.

4.3. *Initial conditions for maximum energy growth at arbitrary locations*

We perform DAL simulations to locate the optimal initial conditions for maximum growth using various location masks $\mathcal{G}$ and time horizons T. The simulations are continued until the gain value G defined as

$$G = \frac{\left\langle \mathcal{G}\tilde{\boldsymbol{u}}'(\boldsymbol{x}, T) \cdot \tilde{\boldsymbol{u}}'(\boldsymbol{x}, T) \right\rangle}{\left\langle \tilde{\boldsymbol{u}}'(\boldsymbol{x}, 0) \cdot \tilde{\boldsymbol{u}}'(\boldsymbol{x}, 0) \right\rangle} \quad (4.9)$$

is converged. Given that the simulations become rather costly for longer times, we start by choosing short horizons T and increase gradually to probe larger time spans. By changing $\mathcal{G}$, we explore whether maximum energy growth at an arbitrary location, e.g. downstream of the leading edge, is linked to an optimal initial condition upstream, perhaps close to the leading edge. Such an analysis would reveal a footprint of the wave maker on the subsequent vorticity generation at any given location.
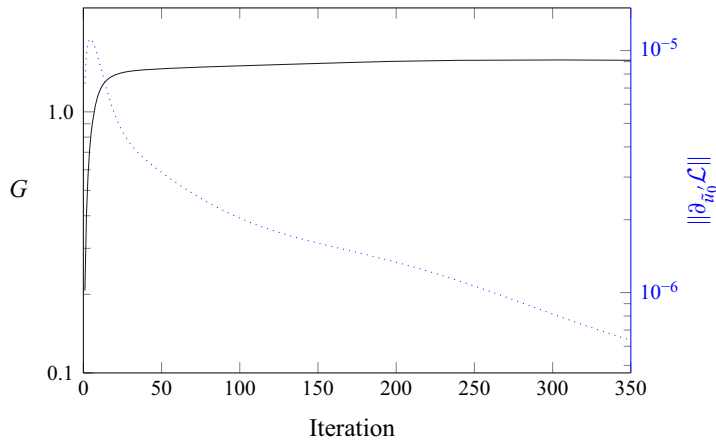
Figure 16. Growth (left axis) and residual (right axis) for the mid-leaflet mask and for $T = 0.01$.

4.3.1. *Maximum energy growth between the leading and trailing edges*

We start by analysing the energy growth between the leading and trailing edges (referred to as mid-leaflet in what follows). This area Ω_v is located downstream of the ILEV zone and overlaps with the wave maker. It is expected that the optimal initial condition will be mainly focused around the leading edge, particularly in the ILEV zone, due to its close proximity and small value of T.

A circular energy probe of radius $R = 3.6$ mm is located at $(\xi, r) = (5.76, 0\ \text{mm})$. DAL simulations are then performed for different times $T = 0.01$, $T = 0.05$ and $T = 0.1$. In contrast to the DAL simulations for channel flow, (see Appendix C) the current simulations require larger numbers of iterations to converge (see figure 16). This may be a consequence of the presence of multiple globally unstable modes in the system, e.g. stemming from the ILEV, cavities and the wake.

Figure 17(*a,b*) shows the initial ($t = 0$) and terminal ($t = T$) states corresponding to maximum energy growth at the mid-leaflet mask and $T = 0.01$ (smallest computed time). Due to the short terminal time, the optimal initial conditions are mainly focused within the mask. This suggests that instability growth for this mask remains almost entirely locally for small time scales. An exploration of instabilities outside the mask requires a larger time horizon T. Panels (*c,d*) and (*e,f*) of figure 17 show results for $T = 0.05$ and $T = 0.1$, respectively. As expected, the optimal initial condition moves towards the leading edge, including a part of the ILEV zone, as T is increased. These results furthermore reveal an additional 'actor' besides the ILEV: the flow impingement zone located on the leaflet's thickness (area upstream of the green dashed line in the bottom row of figure 17). This area displays high potential for creating disturbances that are subsequently amplified by the ILEV. Figure 17(*c–f*) also shows that the initial and terminal states are slightly asymmetric despite the symmetry of the leaflets. This is due to minor differences in the depth of the cavities in the 2-D submodel (Zolfaghari & Obrist 2019), which results in slightly asymmetric ILEV profiles on the upper and lower leaflets.

4.3.2. *Maximum energy growth at the trailing edge*

Next, we displace the mask $\mathscr{G}$ farther downstream, such that it targets the area at the trailing edge of the leaflets. This area was identified by Zolfaghari & Obrist (2019) as
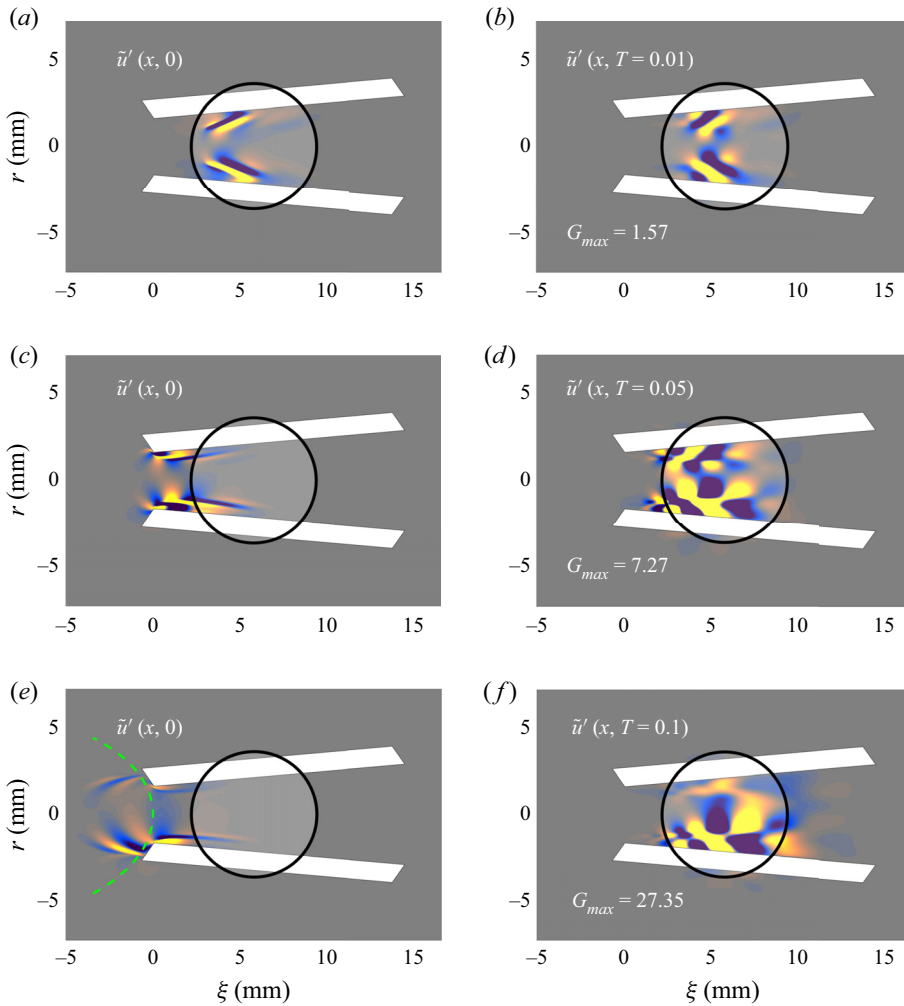
936 A41-22

Figure 17. Streamwise component of (*a,c,e*) optimal initial and (*b,d,f*) final states are demonstrated for a mid-leaflet mask. From top to bottom, cases with $T = 0.01$, $T = 0.05$ and $T = 0.1$ are shown, respectively. The domain within the circle identifies the mask Ω_v. Dark blue and light yellow areas signify minimum negative and maximum positive velocity disturbances, respectively.

the interaction zone where the vorticity waves produced by the ILEV interacted with the wake structures, to ultimately force their breakdown. It is important to explore the possibility of this breakdown, which visually seemed to be caused by ILEV, being additionally driven by other instabilities originating in the cavities or the wake itself.

DAL simulations were performed using a circular energy probe of radius $R = 3.6$ mm located at $(\xi, r) = (14.76, 0 \text{ mm})$. Due to an increased distance from the leading edge, larger times may be needed for revealing the leading-edge signature. For this reason, we performed looping simulations for the mid-leaflet case for a fourth terminal time of $T = 0.2$, in addition to the previous values of $T = 0.01$, $T = 0.05$ and $T = 0.1$.

Figure 18(*a,b*) shows the initial and terminal conditions corresponding to a maximum gain G at trailing edge for $T = 0.01$. Similar to the mid-leaflet mask, for the smallest time,
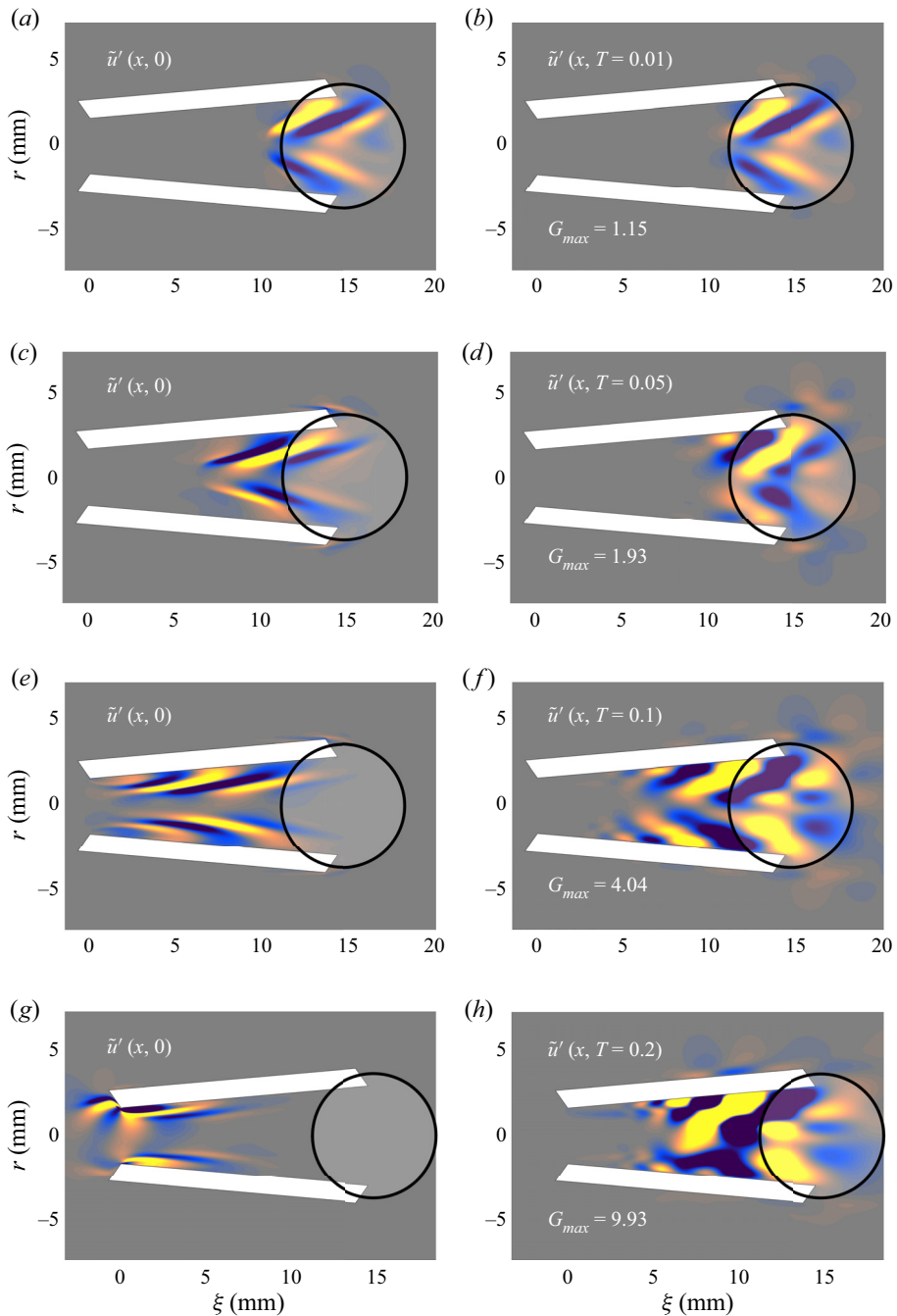
Figure 18. Streamwise component of the (*a*,*c*,*e*,*g*) optimal initial and (*b*,*d*,*f*,*h*) final states are demonstrated for a trailing-edge mask. From top to bottom, cases with $T = 0.01$, $T = 0.05$, $T = 0.1$ and $T = 0.2$ are shown, respectively. The domain within the circle identifies the mask Ω_v. Dark blue and light yellow areas signify minimum negative and maximum positive velocity disturbances, respectively.
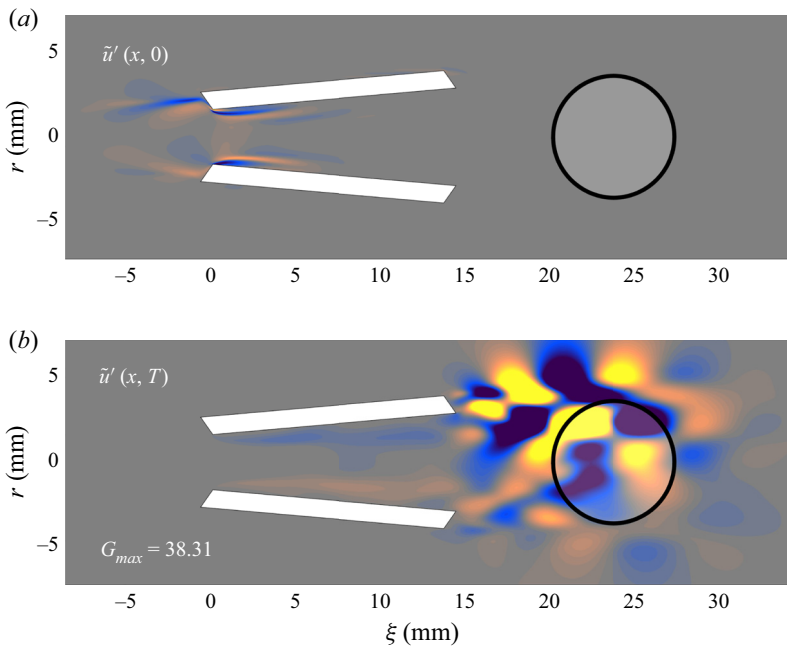
Figure 19. Initial (*a*) and final (*b*) states for a wake mask and a terminal time $T = 0.4$. The domain within the circle identifies the mask Ω_v. Dark blue and light yellow areas indicate the minimum negative and maximum positive velocity disturbances, respectively.

the optimal initial condition is concentrated on the mask itself. However, by increasing the time horizon T, the instability is progressively driven by disturbances created farther upstream (see, from top to bottom the second, third and fourth rows of figure 18). Figure 18(*e, f*) shows that the optimal initial condition mainly consists of Orr structures linked to the shear profile that is formed downstream of the ILEV zone. These structures become skewed within the ILEV zone, due to the specific shape of the velocity profiles in this area (Zolfaghari & Obrist 2019). Figure 18(g,h) is particularly relevant, as it shows that, for sufficiently large T, the initial conditions for maximum energy growth near the trailing edge are mostly influenced by the leading-edge structures, including the ILEV instability.

4.3.3. *Maximum energy growth in the wake region*

Finally, we study the optimal energy growth in the wake area of the 2-D BMHV submodel. To this end, we place Ω_v downstream of the trailing edge where growth can be influenced by upstream wake structures as well as other instability mechanisms such as those arising from the cavities.

The DAL simulations were performed using a circular energy probe of radius $R = 3.6$ mm located at $(\xi, r) = (23.7, 0 \text{ mm})$. Figure 19 shows the initial condition for maximum energy growth at this location. Given a sufficiently long time $T = 0.4$, the maximum growth for this area is driven by an optimal initial condition originating at the leading edge. This is an important observation, as it verifies the crucial role the leading-edge design of the leaflet plays on the disturbance energy growth, triggering or promoting turbulent flow features in the wake of the valve. This phenomenon has been observed in Zolfaghari & Obrist (2019), but is verified quantitatively here. A 3-D transient

growth analysis, regardless of prohibitive computational costs, is unlikely to change the key outcome here, that is, the energy growth in the wake is promoted mainly by ILEV mechanism. This is supported by DNS evidence (see figure 7) where elimination of ILEV significantly reduced the turbulence in the wake of the valve, while other instability mechanisms were present.

4.4. *Computational aspects of the adjoint-looping simulations*

All BMHV DAL simulations presented above were performed on the 2-D BMHV submodel of Zolfaghari & Obrist (2019). The computational domain including the aortic root and the valve model was discretised using $1025 \times 5120 \approx 5.24M$ grid points. Such high resolution is necessary to resolve the ILEV instabilities (Zolfaghari & Obrist 2019). DAL simulations proved to be computationally demanding, even for the 2-D model. As can be seen from figure 16, 300 iterations were needed for convergence, using a fixed step size for updating the initial condition at each iteration. DNSs were performed using a time-step size of $dt = 0.0005$, while a smaller time-step size of approximately $dt = 0.0002$ (for the backward in time integration) was used for the adjoint simulations to ensure numerical stability. The cost of one iteration in the DAL procedure was hence 3.5 times the cost of a DNS.

The computational cost was considerable for larger values of the terminal time T. For instance, 2034 core hours were needed to complete 50 iterations with the farthest downstream mask (cf. § 4.3.3), using the Haswell nodes of the Cray XC40/50 supercomputer (*Piz Daint*).

5. Conclusions

This study presented results from an analysis of the structural sensitivity and downstream influence of the impinging leading-edge instability in a BMHV. The ILEV instability mechanism has been shown previously to contribute strongly to the onset and intensity of turbulent flow past a 2-D BMHV submodel using local linear instability theory and 2-D DNS. Here, we first use 3-D DNS to show the significant influence of the ILEV mechanism on the laminar–turbulent transition in BMHV flow. Then, we investigate the 2-D global instability of the ILEV flow using a 2-D submodel taken from Zolfaghari & Obrist (2019). We subsequently performed a sensitivity analysis using adjoints of the global modes with the aim of designing a passive device to reduce the impact of ILEV instabilities on the wake flow. We introduced small bluff bodies into the BMHV flow at areas of high sensitivity as means to stabilise the identified global modes. The efficiency of this attempt has been tested using 2-D DNS. Finally, an extension of our instability analysis to take into account the effect of alternative instability mechanisms in the flow concluded our analysis. Using a non-modal approach, we sought to (i) clarify the role of ILEV on energy growth leading to increased turbulent effects in the wake of the valve, particularly, in the presence of other mechanisms, (ii) understand the time-dependent growth mechanisms leading to instability at locations of interest and (iii) create a generalised model for efficient control strategies to reduce the influence of ILEV flow on the wake.

Even though Zolfaghari & Obrist (2019) identified a pocket of absolute instability in the BMHV flow, local theory could not produce targeted control strategies for reducing the ILEV instability. These configurations often require a global approach. As such a 2-D global instability mechanism can provide the structure of 2-D unstable modes, for which suitable control scenarios can be designed. This global approach may also provide

the necessary flexibility for studying other types of modifications, which is especially important for a prosthetic heart-valve design that is constrained by physiological and manufacturing restrictions. In line with this rationale, we extended the local analysis of Zolfaghari & Obrist (2019) to a 2-D global analysis that incorporated the entire span of the ILEV flow. We investigated the temporal instability of mean ILEV flow profiles. Two zero-frequency unstable modes were identified for this flow, in agreement with the existence of a wave maker, as shown in Zolfaghari & Obrist (2019). We then attempted to stabilise these modes by introducing local feedbacks (e.g. small bluff bodies, see Hill 1992) into the flow. To this end, the structural sensitivity of the identified globally unstable modes has been assessed based on their adjoints. Areas of high sensitivity in the ILEV zone included an area upstream of the wave-maker zone (identified using a local stability analysis) for one mode, and a second part approximately within the wave-maker zone. The same sensitivity analysis was employed to probe the placement of small momentum feedback as a roughness element on the valve leaflet, and the resulting modified flow was investigated by 2-D DNS. Our results showed a notable reduction in vorticity production between the leaflets and in the wake for one mode. For the second mode, the momentum feedback enhanced the instability, and the resulting flow was more chaotic. In essence, we demonstrated that by triggering only one mode, the instability can diminished, but not fully suppressed.

We proceeded by developing a model to investigate the effect of the ILEV zone on transient energy growth in the BMHV model. This analysis was based on a cost functional to identify optimal initial conditions for maximum energy growth in selected areas in the flow domain and over specific time horizons. Coupled with an adjoint-looping simulation code and considering the full flow domain including cavities and wake regions, we showed that, for sufficiently large times, the optimal initial conditions for maximal energy growth in the wake, the trailing edge and between the leaflets concentrated around the leading edge of the valve. This identified area further breaks down in a part upstream of the leaflets (marked by flow impingement due to the thickness of the valve leaflets) and a part downstream of the leading edge (marked by the ILEV mechanism).

Even though based on simplifying assumptions about the valve system, this present study represents a primary and encouraging step towards employing gradient-based approaches for uncovering the sources of instabilities in complex biomedical systems, such as the blood flow about a prosthetic heart-valve configuration. It also provides the necessary groundwork for future attempts on deploying these gradient-based methodologies for suppressing the unphysiological instabilities in these prostheses.

Declaration of interests. The authors report no conflict of interest.

Author ORCIDs.

- Hadi Zolfaghari https://orcid.org/0000-0002-0953-5939;
- Rich R. Kerswell https://orcid.org/0000-0001-5460-5337;
- Dominik Obrist https://orcid.org/0000-0002-6062-9076;
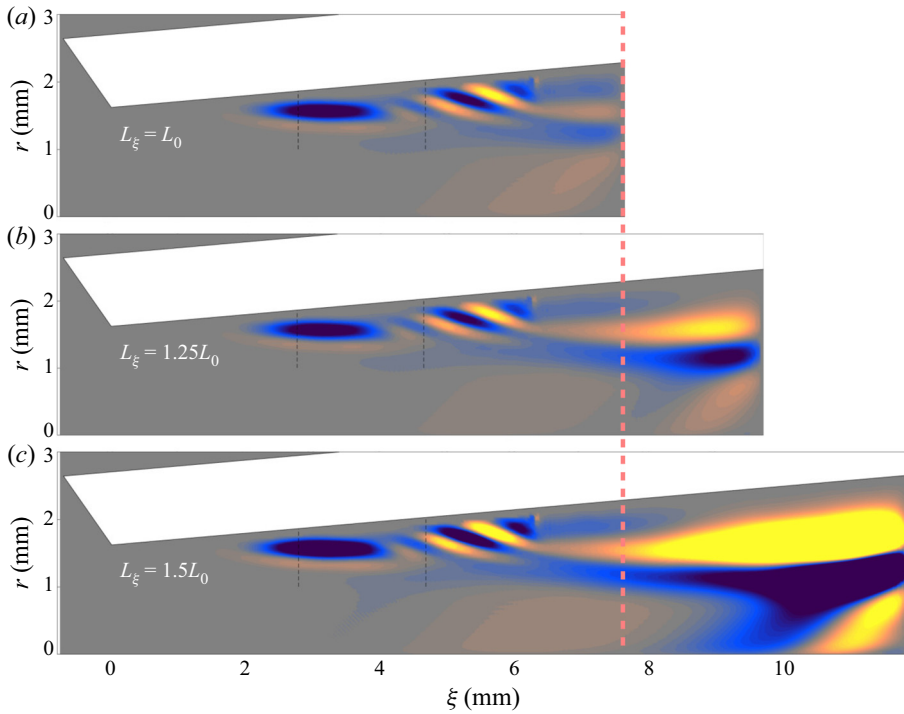- Peter J. Schmid https://orcid.org/0000-0002-2257-8490.

Figure 20. Independence of the structure of mode A ($\tilde{\beta} = 0.00181\mathrm{i}$) from the location of outflow boundary. From top to bottom, the modes are calculated for domain longitudinal extents of L_0 (original case), $1.25L_0$ and $1.5L_0$.

Appendix A. Validation of global modes subject to domain truncation: influence of outflow boundary

Here, we show that the global modes A and B obtained in § 3 are not affected when the position of outflow boundary is moved downstream. The domain length (referred to as L_ξ which was set to $L_0 = 7.69$ mm in § 3) is increased by 25 % and 50 % and the unstable modes A and B are computed. Figures 20 and 21 show that such extension does not affect the structure of the modes within $L_\xi = L_0$. Further, their associated eigenvalues, i.e. $\tilde{\beta} = 0.00181\mathrm{i}$ for mode A and $\tilde{\beta} = 0.00175\mathrm{i}$ for mode B, remain the same as well.

Appendix B. Adjoint of the LNSE with geometric masks

Taking the first variation of $\mathcal{L}$ with respect to $\tilde{p}'$, using the integration by parts, gives

$$\left(\frac{\delta\mathcal{L}}{\delta\tilde{p}'}, \delta\tilde{p}'\right) = \int_0^{\mathrm{T}} \left\langle \tilde{u}'^{,\ddagger} \cdot \nabla\delta\tilde{p}' \right\rangle \mathrm{d}t = \int_0^{\mathrm{T}} \left\langle \nabla \cdot (\tilde{u}'^{,\ddagger}\delta\tilde{p}') \right\rangle \mathrm{d}t - \int_0^{\mathrm{T}} \left\langle \delta\tilde{p}'(\nabla \cdot \tilde{u}'^{,\ddagger}) \right\rangle \mathrm{d}t. \quad \text{(B1)}$$

This expression vanishes, if $\tilde{u}'^{,\ddagger}$ vanishes at the domain boundaries, resulting in

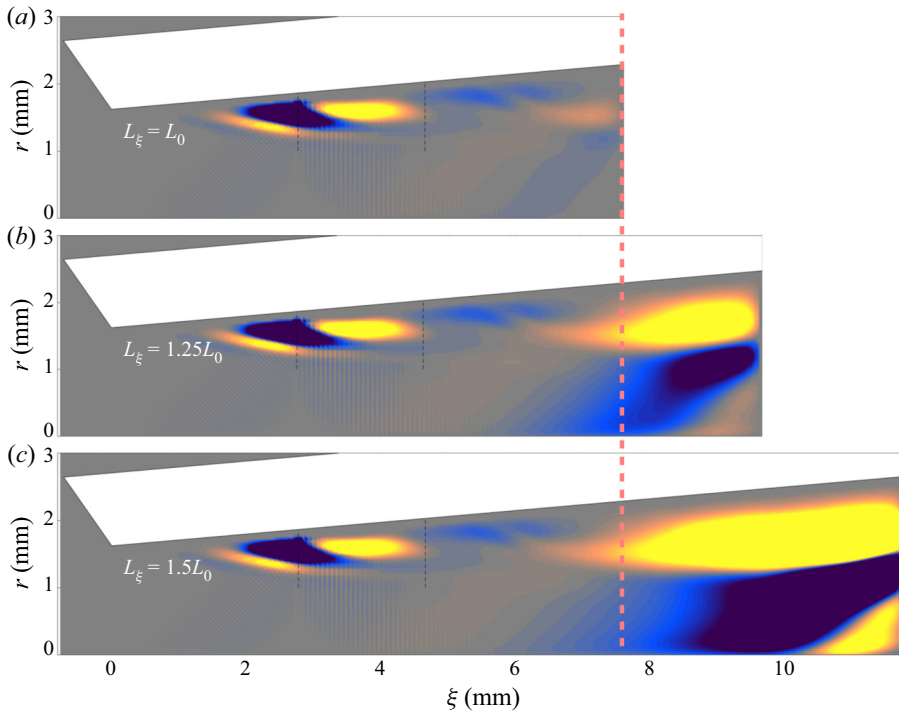$$\nabla \cdot \tilde{u}'^{,\ddagger} = 0, \quad \text{(B2)}$$

Figure 21. Independence of the structure of mode B ($\tilde{\beta} = 0.00175i$) from the location of outflow boundary. From top to bottom, the modes are calculated for domain longitudinal extents of L_0 (original case), $1.25L_0$ and $1.5L_0$.

thus confirming that the adjoint velocity field $\tilde{u}'^{,\ddagger}$ is also incompressible. Next, we consider the first variation of $\mathcal{L}$ with respect to $\tilde{u}'$

$$
\left(\frac{\delta \mathcal{L}}{\delta \tilde{u}'}, \delta \tilde{u}' \right) = \left\langle \mathcal{G} \tilde{u}'(x, T) \cdot \delta \tilde{u}'(x, T) \right\rangle + \phi \left\{ \left\langle \tilde{u}'(x, 0) \cdot \delta \tilde{u}'(x, 0) \right\rangle \right\}
$$

$$
+ \int_0^T \left\langle \tilde{u}'^{,\ddagger} \cdot \{ \partial_t \delta \tilde{u}' + \delta \tilde{u}' \cdot \nabla \tilde{U} + \tilde{U} \cdot \nabla \delta \tilde{u}' + Re^{-1} \nabla^2 \delta \tilde{u}' \} \right\rangle \mathrm{d}t + \int_0^T \left\langle \tilde{p}'^{,\ddagger} \nabla \cdot \delta \tilde{u}' \right\rangle \mathrm{d}t.
$$
(B3)

Note that, when taking the variation of the first term in the objective $\mathcal{J}_{\mathcal{G}, E_0}$, we used the following property of the geometric mapping function $\mathcal{G}$:

$$
\left\langle \mathcal{G} \delta \tilde{u}' \cdot \mathcal{G} \delta \tilde{u}' \right\rangle = \left\langle \delta \tilde{u}' \cdot \mathcal{G} \delta \tilde{u}' \right\rangle = \left\langle \mathcal{G} \delta \tilde{u}' \cdot \delta \tilde{u}' \right\rangle.
$$
(B4)

The first and second integrals over the time period $[0, T]$ can be simplified using integration by parts as follows. The first term of the first integral becomes

$$
\int_0^T \left\langle \tilde{u}'^{,\ddagger} \cdot \partial_t \delta \tilde{u}' \right\rangle \mathrm{d}t = \int_0^T \partial_t \left\langle \tilde{u}'^{,\ddagger} \cdot \delta \tilde{u}' \right\rangle \mathrm{d}t - \int_0^T \left\langle \partial_t \tilde{u}'^{,\ddagger} \cdot \delta \tilde{u}' \right\rangle \mathrm{d}t
$$

$$
= \left\langle \tilde{u}'^{,\ddagger}(T) \cdot \delta \tilde{u}'(T) \right\rangle - \left\langle \tilde{u}'^{,\ddagger}(0) \cdot \delta \tilde{u}'(0) \right\rangle - \int_0^T \left\langle \partial_t \tilde{u}'^{,\ddagger} \cdot \delta \tilde{u}' \right\rangle \mathrm{d}t.
$$
(B5)

For proceeding with the second, third, fourth and fifth terms, we use the following identities for an arbitrary vector $\tilde{\boldsymbol{a}}$ with the same size as $\tilde{\boldsymbol{u}}'$

$$
\begin{aligned}
\left\langle \tilde{\boldsymbol{u}}'^{,\ddagger} \cdot \{\tilde{\boldsymbol{a}} \cdot \nabla \delta \tilde{\boldsymbol{u}}'\} \right\rangle &= \left\langle \nabla \cdot \{(\tilde{\boldsymbol{u}}'^{,\ddagger} \cdot \delta \tilde{\boldsymbol{u}}')\tilde{\boldsymbol{a}}\} \right\rangle - \left\langle \tilde{\boldsymbol{u}}' \cdot \{\tilde{\boldsymbol{a}} \cdot \nabla \tilde{\boldsymbol{u}}'^{,\ddagger}\} \right\rangle \\
&= \int_{\partial \Omega} (\tilde{\boldsymbol{u}}'^{,\ddagger} \cdot \delta \tilde{\boldsymbol{u}}')\tilde{\boldsymbol{a}} \, \mathrm{d}S - \left\langle \tilde{\boldsymbol{u}}' \cdot \{\tilde{\boldsymbol{a}} \cdot \nabla \tilde{\boldsymbol{u}}'^{,\ddagger}\} \right\rangle = - \left\langle \tilde{\boldsymbol{u}}' \cdot \{\tilde{\boldsymbol{a}} \cdot \nabla \tilde{\boldsymbol{u}}'^{,\ddagger}\} \right\rangle,
\end{aligned} \tag{B6}
$$

and

$$
\left\langle \tilde{\boldsymbol{u}}'^{,\ddagger} \cdot \{(\delta \tilde{\boldsymbol{u}}' \cdot \nabla)\tilde{\boldsymbol{a}}\} \right\rangle = \left\langle \delta \tilde{\boldsymbol{u}}' \cdot \{\tilde{\boldsymbol{u}}'^{,\ddagger} \cdot (\nabla \tilde{\boldsymbol{a}})^{\mathrm{T}}\} \right\rangle. \tag{B7}
$$

The viscous term, using Green's second identity, can be written as

$$
\begin{aligned}
\int_0^{\mathrm{T}} \left\langle \tilde{\boldsymbol{u}}'^{,\ddagger} \cdot \{-Re^{-1}\nabla^2 \tilde{\boldsymbol{u}}'\} \right\rangle \mathrm{d}t &= -Re^{-1} \int_0^{\mathrm{T}} \left\langle \tilde{\boldsymbol{u}}'^{,\ddagger} \cdot \nabla^2 \tilde{\boldsymbol{u}}' \right\rangle \mathrm{d}t \\
&= -Re^{-1} \int_0^{\mathrm{T}} \left\langle \tilde{\boldsymbol{u}}' \cdot \nabla^2 \tilde{\boldsymbol{u}}'^{,\ddagger} \right\rangle \mathrm{d}t + \int_0^{\mathrm{T}} \int_{\partial \Omega} \tilde{\boldsymbol{u}}'^{,\ddagger} \cdot \frac{\partial \tilde{\boldsymbol{u}}'}{\partial \tilde{\boldsymbol{n}}} \mathrm{d}S \, \mathrm{d}t + \int_0^{\mathrm{T}} \int_{\partial \Omega} \tilde{\boldsymbol{u}}' \cdot \frac{\partial \tilde{\boldsymbol{u}}'^{,\ddagger}}{\partial \tilde{\boldsymbol{n}}} \mathrm{d}S \, \mathrm{d}t \\
&= -Re^{-1} \int_0^{\mathrm{T}} \left\langle \tilde{\boldsymbol{u}}' \cdot \nabla^2 \tilde{\boldsymbol{u}}'^{,\ddagger} \right\rangle \mathrm{d}t,
\end{aligned} \tag{B8}
$$

where $\tilde{\boldsymbol{n}}$ is the unit vector normal to the domain surface S. Lastly, the second time integral is integrated by parts to yield

$$
\begin{aligned}
\int_0^{\mathrm{T}} \left\langle \tilde{p}'^{,\ddagger} \cdot \{\nabla \cdot \tilde{\boldsymbol{u}}'\} \right\rangle &= \int_0^{\mathrm{T}} \left\langle \nabla \cdot \{\tilde{p}'^{,\ddagger} \delta \tilde{\boldsymbol{u}}'\} \right\rangle \mathrm{d}t - \int_0^{\mathrm{T}} \left\langle \delta \tilde{\boldsymbol{u}}' \cdot \nabla \tilde{p}'^{,\ddagger} \right\rangle \mathrm{d}t \\
&= \int_0^{\mathrm{T}} \int_{\partial \Omega} \tilde{p}'^{,\ddagger} \delta \tilde{\boldsymbol{u}}' \mathrm{d}S \, \mathrm{d}t - \int_0^{\mathrm{T}} \left\langle \delta \tilde{\boldsymbol{u}}' \cdot \nabla \tilde{p}'^{,\ddagger} \right\rangle \mathrm{d}t = - \int_0^{\mathrm{T}} \left\langle \delta \tilde{\boldsymbol{u}}' \cdot \nabla \tilde{p}'^{,\ddagger} \right\rangle \mathrm{d}t.
\end{aligned} \tag{B9}
$$

Substituting all reformulated terms for the first and second time integrals into (B3), we obtain

$$
\begin{aligned}
\left(\frac{\delta \mathcal{L}}{\delta \tilde{\boldsymbol{u}}'}, \delta \tilde{\boldsymbol{u}}' \right) &= \left\langle \mathcal{G} \tilde{\boldsymbol{u}}'(\boldsymbol{x}, T) \cdot \delta \tilde{\boldsymbol{u}}'(\boldsymbol{x}, T) \right\rangle + \phi \left\{ \left\langle \tilde{\boldsymbol{u}}'(\boldsymbol{x}, 0) \cdot \delta \tilde{\boldsymbol{u}}'(\boldsymbol{x}, 0) \right\rangle \right\} \\
&\quad + \left\langle \tilde{\boldsymbol{u}}'^{,\ddagger}(\boldsymbol{x}, T) \cdot \delta \tilde{\boldsymbol{u}}'(\boldsymbol{x}, T) \right\rangle - \left\langle \tilde{\boldsymbol{u}}'^{,\ddagger}(\boldsymbol{x}, 0) \cdot \delta \tilde{\boldsymbol{u}}'(\boldsymbol{x}, 0) \right\rangle \\
&\quad - \int_0^{\mathrm{T}} \left\langle \partial_t \tilde{\boldsymbol{u}}'^{,\ddagger} \cdot \delta \tilde{\boldsymbol{u}}' - \delta \tilde{\boldsymbol{u}}' \cdot \{\tilde{\boldsymbol{U}} \cdot \nabla \tilde{\boldsymbol{u}}'^{,\ddagger}\} \right. \\
&\quad \left. + \delta \tilde{\boldsymbol{u}}' \cdot \{\tilde{\boldsymbol{u}}'^{,\ddagger} \cdot (\nabla \tilde{\boldsymbol{U}})^{\mathrm{T}}\} - Re^{-1} \delta \tilde{\boldsymbol{u}}' \cdot \nabla^2 \tilde{\boldsymbol{u}}'^{,\ddagger} + \delta \tilde{\boldsymbol{u}}' \cdot \nabla \tilde{p}'^{,\ddagger} \right\rangle \mathrm{d}t.
\end{aligned} \tag{B10}
$$

Appendix C. Validation of the linear DAL calculation

Our validation closely follows the analysis of maximum linear energy growth in plane Poiseuille flow performed by Reddy & Henningson (1993). The base flow $\tilde{\boldsymbol{U}} = (1 - y^2, 0)\hat{\boldsymbol{x}}$ is considered across the channel $(x, y) \in [0, 2\pi] \times [-1, 1]$. Substituting this base flow into the LNSE and performing a Fourier transform using the ansatz $\tilde{\boldsymbol{q}}'(x, y, t) =$
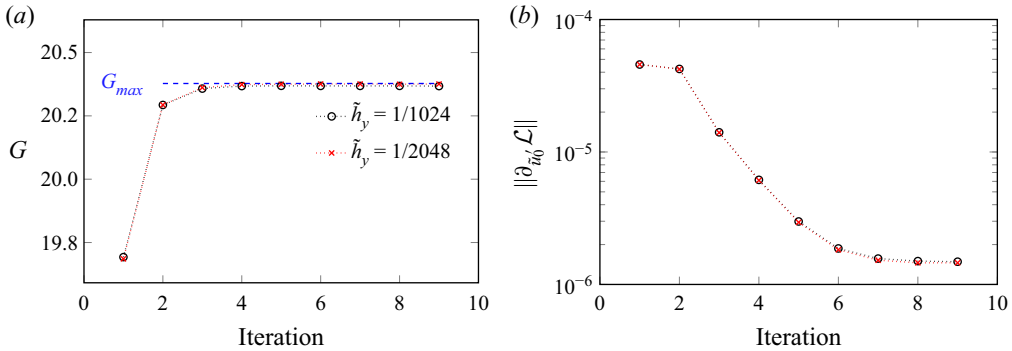
Figure 22. Growth (*a*) and residual (*b*) for the adjoint looping simulation for plane channel flow at $Re = 3000$ and $\alpha = 1$. The calculated value for the maximum growth based on eigenfunctions is shown on the panel *a* as G_{max}.

$\hat{\boldsymbol{q}}(y) \exp(\mathrm{i}(\tilde{\gamma}t + \alpha x))$, results in

$$
\begin{bmatrix}
\mathscr{L}\{\tilde{\boldsymbol{U}}; Re\} & 2y & -\mathrm{i}\alpha \\
0 & \mathscr{L}\{\tilde{\boldsymbol{U}}; Re\} & -\mathscr{D}_y \\
\mathscr{D}_x & \mathscr{D}_y & 0
\end{bmatrix}
\begin{bmatrix}
\hat{u} \\
\hat{v} \\
\hat{p}
\end{bmatrix}
= \mathrm{i}\tilde{\gamma}
\begin{bmatrix}
1 & 0 & 0 \\
0 & 1 & 0 \\
0 & 0 & 0
\end{bmatrix}
\begin{bmatrix}
\hat{u} \\
\hat{v} \\
\hat{p}
\end{bmatrix} \tag{C1}
$$

where $\mathscr{L}\{\tilde{\boldsymbol{U}}; Re\} = -\mathrm{i}\alpha(1 - y^2) + 1/Re(\mathscr{D}_{yy} - \alpha^2)$; $\hat{\boldsymbol{q}} = (\hat{\boldsymbol{u}}, \hat{p})$ and $\hat{\boldsymbol{u}} = (\hat{u}, \hat{v})$. The operators $\mathscr{D}_y$, and $\mathscr{D}_{yy}$ denote the first and second derivatives in the wall-normal direction, respectively.

Equation (C1) is solved using a Chebyshev spectral collocation method (Clenshaw 1957). To save computational time, only half the channel height ($0 \leq y \leq 1$) is considered, resorting to the case where $\hat{v}$ is symmetric and $\hat{u}$ and $\hat{p}$ are antisymmetric for the known optimal solution. The collocation points y_i with

$$
y_i = \cos\left(\frac{(i - 1/2)\pi}{2N + 1}\right) \tag{C2}
$$

are taken as the roots of the Chebyshev polynomial of degree $2N + 1$ (T_{2N+1}).

Following Reddy & Henningson (1993) the maximum growth at time T was then calculated as

$$
G_{max,K}(\alpha, Re, T) = \sup_{\forall \hat{\boldsymbol{u}}(y, t=0)} \frac{\left\| \hat{\boldsymbol{u}}_K(y, t = T) \right\|_2^2}{\left\| \hat{\boldsymbol{u}}_K(y, t = 0) \right\|_2^2}, \tag{C3}
$$

where K is the number of eigenfunctions used in an expansion of $\hat{\boldsymbol{u}}(y, t)$

$$
\hat{\boldsymbol{u}}_K(y, t) = \sum_{i=1}^{K} a_i \, \mathrm{e}^{\mathrm{i}\gamma_i t} \hat{\boldsymbol{u}}_i(y). \tag{C4}
$$

The eigenfunctions are ordered by growth rate γ_i. For sufficiently large K, $G_{max,K}$ converges to G_{max} for a given T. For $Re = 3000$ and $\alpha = 1$, a maximum gain of $G_{max} = 20.3625$ was obtained for time $T = 15$. Convergence was achieved using $K = 40$ eigenfunctions in the expansion of $\hat{\boldsymbol{u}}_K(y, t = T)$.

Figure 22 shows the gain G and the residual $\left\| \partial_{\tilde{u}'(0)} \mathcal{L} \right\|$ for the iterations of two simulations with wall-normal resolutions of 1024 and 2048. The *simulated* maximum
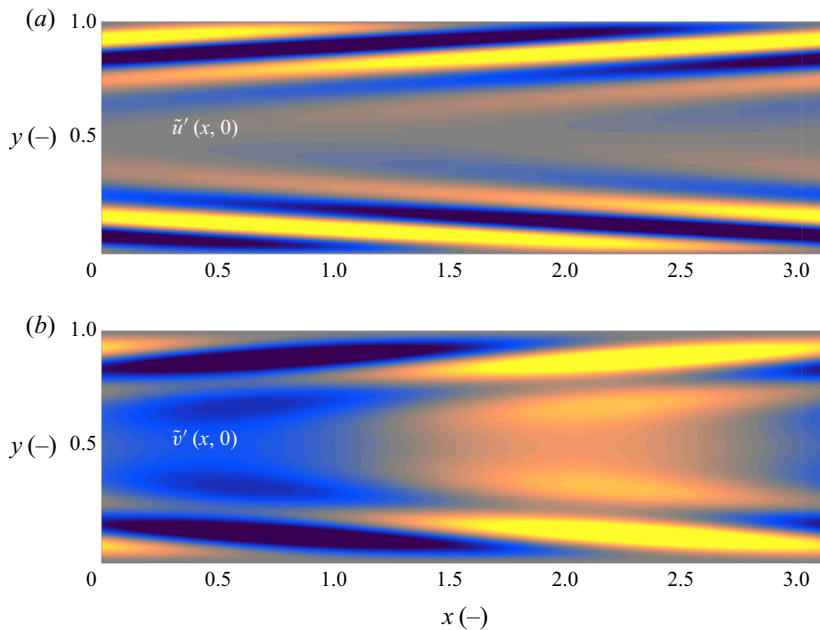
(*a*)

(*b*)

Figure 23. Optimal initial conditions for the maximum energy growth for disturbances with $\alpha = 1$ at time $T = 15$ in plane channel flow at $Re = 3000$. Colours are magnified tenfold for $\tilde{v}'(\boldsymbol{x}, 0)$ for visualisation clarity.

growth of $G_{max,s} = 20.3605$ was obtained at a resolution of 2048 points. This value corresponds to a relative error of 0.009 %. The optimal initial conditions obtained from the adjoint looping simulation are given in figure 23.

REFERENCES

ALEMU, Y. & BLUESTEIN, D. 2007 Flow-induced platelet activation and damage accumulation in a mechanical heart valve: numerical studies. *Artif. Organs* **31** (9), 677–688.

BELLOFIORE, A., DONOHUE, E.M. & QUINLAN, N.J. 2011 Scale-up of an unsteady flow field for enhanced spatial and temporal resolution of PIV measurements: application to leaflet wake flow in a mechanical heart valve. *Exp. Fluids* **51** (1), 161–176.

BORAZJANI, I., GE, L. & SOTIROPOULOS, F. 2008 Curvilinear immersed boundary method for simulating fluid structure interaction with complex 3D rigid bodies. *J. Comput. Phys.* **227** (16), 7587–7620.

CHERRY, N.J., HILLIER, R. & LATOUR, M.E.M.P. 1984 Unsteady measurements in a separated and reattaching flow. *J. Fluid Mech.* **144**, 13–46.

CLENSHAW, C.W. 1957 *The Numerical Solution of Linear Differential Equations in Chebyshev Series*. Philosophical Society. pp. 134–149

DASI, L.P., GE, L., SIMON, H.A., SOTIROPOULOS, F. & YOGANATHAN, A.P. 2007 Vorticity dynamics of a bileaflet mechanical heart valve in an axisymmetric aorta. *Phys. Fluids* **19** (6), 067105.

DENIZ, S. & STAUBLI, T. 1997 Oscillating rectangular and octagonal profiles: interaction of leading-and trailing-edge vortex formation. *J. Fluids Struct.* **11** (1), 3–31.

GE, L., DASI, L.P., SOTIROPOULOS, F. & YOGANATHAN, A.P. 2008 Characterization of hemodynamic forces induced by mechanical heart valves: Reynolds vs. viscous stresses. *Ann. Biomed. Engng* **36** (2), 276–297.

GIANNETTI, F. & LUCHINI, P. 2007 Structural sensitivity of the first instability of the cylinder wake. *J. Fluid Mech.* **581**, 167–197.

HATOUM, H. & DASI, L.P. 2019 Reduction of pressure gradient and turbulence using vortex generators in prosthetic heart valves. *Ann. Biomed. Engng* **47** (1), 85–96.

HATOUM, H., VALLABHUNENI, S., KOTA, A.K., BARK, D.L., POPAT, K.C. & DASI, L.P. 2020 Impact of superhydrophobicity on the fluid dynamics of a bileaflet mechanical heart valve. *J. Mech. Behav. Biomed. Mater.* **110**, 103895.

HAYA, L. & TAVOULARIS, S. 2016 Effects of bileaflet mechanical heart valve orientation on fluid stresses and coronary flow. *J. Fluid Mech.* **806**, 129–164.

HEDAYAT, M., ASGHARZADEH, H. & BORAZJANI, I. 2017 Platelet activation of mechanical versus bioprosthetic heart valves during systole. *J. Biomech.* **56**, 111–116.

HEDAYAT, M. & BORAZJANI, I. 2019 Comparison of platelet activation through hinge vs bulk flow in bileaflet mechanical heart valves. *J. Biomech.* **83**, 280–290.

HENNIGER, R., KLEISER, L. & MEIBURG, E. 2010*a* Direct numerical simulations of particle transport in a model estuary. *J. Turbul.* **11**, N39.

HENNIGER, R., OBRIST, D. & KLEISER, L. 2010*b* High-order accurate solution of the incompressible Navier–Stokes equations on massively parallel computers. *J. Comput. Phys.* **229** (10), 3543–3572.

HILL, D. 1992 A theoretical approach for analyzing the restabilization of wakes. In *30th Aerospace Sciences Meeting and Exhibit*, p. 67.

HOLME, P.A., ØRVIM, U., HAMERS, M.J.A.G., SOLUM, N.O., BROSSTAD, F.R., BARSTAD, R.M. & SAKARIASSEN, K.S. 1997 Shear-induced platelet activation and platelet microparticle formation at blood flow conditions as in arteries with a severe stenosis. *Arterioscler. Thromb. Vasc. Biol.* **17** (4), 646–653.

HOURIGAN, K., THOMPSON, M.C. & TAN, B.T. 2001 Self-sustained oscillations in flows around long blunt plates. *J. Fluids Struct.* **15** (3-4), 387–398.

IUNG, B. & VAHANIAN, A. 2011 Epidemiology of valvular heart disease in the adult. *Nat. Rev. Cardiol.* **8** (3), 162–172.

JOHN, M.O., OBRIST, D. & KLEISER, L. 2014 Stabilisation of subcritical bypass transition in the leading-edge boundary layer by suction. *J. Turbul.* **15** (11), 795–805.

JOHN, M.O., OBRIST, D. & KLEISER, L. 2016 Secondary instability and subcritical transition of the leading-edge boundary layer. *J. Fluid Mech.* **792**, 682–711.

KUPFER, K., BERS, A. & RAM, A.K. 1987 The cusp map in the complex-frequency plane for absolute instabilities. *Phys. Fluids* **30** (10), 3075–3082.

LASHGARI, I., TAMMISOLA, O., CITRO, V., JUNIPER, M.P. & BRANDT, L. 2014 The planar x-junction flow: stability analysis and control. *J. Fluid Mech.* **753**, 1–28.

MITTAL, R., DONG, H., BOZKURTTAS, M., NAJJAR, F.M., VARGAS, A. & VON LOEBBECKE, A. 2008 A versatile sharp interface immersed boundary method for incompressible flows with complex boundaries. *J. Comput. Phys.* **227** (10), 4825–4852.

MITTAL, R. & IACCARINO, G. 2005 Immersed boundary methods. *Annu. Rev. Fluid Mech.* **37**, 239–261.

NAUDASCHER, E. & WANG, Y. 1993 Flow-induced vibrations of prismatic bodies and grids of prisms. *J. Fluids Struct.* **7** (4), 341–373.

NORDSTRÖM, J., NORDIN, N. & HENNINGSON, D. 1999 The fringe region technique and the fourier method used in the direct numerical simulation of spatially evolving viscous flows. *SIAM J. Sci. Comput.* **20** (4), 1365–1393.

OBRIST, D., HENNIGER, R. & KLEISER, L. 2012 Subcritical spatial transition of swept Hiemenz flow. *Intl J. Heat Fluid Flow* **35**, 61–67.

QUINLAN, N.J. & DOOLEY, P.N. 2007 Models of flow-induced loading on blood cells in laminar and turbulent flow, with application to cardiovascular device flow. *Ann. Biomed. Engng* **35** (8), 1347–1356.

REDDY, S.C. & HENNINGSON, D.S. 1993 Energy growth in viscous channel flows. *J. Fluid Mech.* **252**, 209–238.

SCHMID, P.J. 2007 Nonmodal stability theory. *Annu. Rev. Fluid Mech.* **39**, 129–162.

SCHMID, P.J., DE PANDO, M.F. & PEAKE, N. 2017 Stability analysis for *n*-periodic arrays of fluid systems. *Phys. Rev. Fluids* **2** (11), 113902.

SORIA, J. & WU, J. 1992 The character of the instability of the separated shear layer from a square leading edge flat plate. In *Proceedings of 11th Australasian Fluid Mechanics Conference*, pp. 14–18.

SOTIROPOULOS, F., LE, T.B. & GILMANOV, A. 2016 Fluid mechanics of heart valves and their replacements. *Annu. Rev. Fluid Mech.* **48**, 259–283.

STRYKOWSKI, P.J. & SREENIVASAN, K.R. 1990 On the formation and suppression of vortex 'shedding' at low Reynolds numbers. *J. Fluid Mech.* **218**, 71–107.

THEOFILIS, V. 2011 Global linear instability. *Annu. Rev. Fluid Mech.* **43**, 319–352.

VENNEMANN, B., RÖSGEN, T., HEINISCH, P.P. & OBRIST, D. 2018 Leaflet kinematics of mechanical and bioprosthetic aortic valve prostheses. *ASAIO J.* **64** (5), 651–661.

YOGANATHAN, A.P., HE, Z. & CASEY, J.S. 2004 Fluid mechanics of heart valves. *Annu. Rev. Biomed. Engng* **6**, 331–362.

YUN, B.M., DASI, L.P., AIDUN, C.K. & YOGANATHAN, A.P. 2014*a* Highly resolved pulsatile flows through prosthetic heart valves using the entropic Lattice–Boltzmann method. *J. Fluid Mech.* **754**, 122–160.

YUN, B.M., MCELHINNEY, D.B., ARJUNON, S., MIRABELLA, L., AIDUN, C.K. & YOGANATHAN, A.P. 2014*b* Computational simulations of flow dynamics and blood damage through a bileaflet mechanical heart valve scaled to pediatric size and flow. *J. Biomech.* **47** (12), 3169–3177.

YUN, B.M., WU, J., SIMON, H.A., ARJUNON, S., SOTIROPOULOS, F., AIDUN, C.K. & YOGANATHAN, A.P. 2012 A numerical investigation of blood damage in the hinge area of aortic bileaflet mechanical heart valves during the leakage phase. *Ann. Biomed. Engng* **40** (7), 1468–1485.

ZOLFAGHARI, H., BECSEK, B., NESTOLA, M.G.C., SAWYER, W.B., KRAUSE, R. & OBRIST, D. 2019 High-order accurate simulation of incompressible turbulent flows on many parallel GPUs of a hybrid-node supercomputer. *Comput. Phys. Commun.* **244**, 132–142.

ZOLFAGHARI, H., IZBASSAROV, D. & MURADOGLU, M. 2017 Simulations of viscoelastic two-phase flows in complex geometries. *Comput. Fluids* **156**, 548–561.

ZOLFAGHARI, H. & OBRIST, D. 2019 Absolute instability of impinging leading edge vortices in a submodel of a bileaflet mechanical heart valve. *Phys. Rev. Fluids* **4** (12), 123901.

ZOLFAGHARI, H. & OBRIST, D. 2021 A high-throughput hybrid task and data parallel poisson solver for large-scale simulations of incompressible turbulent flows on distributed GPUs. *J. Comput. Phys.* **437**, 110329.